Engineering Structures 49 (2013) 202–220

Contents lists available at SciVerse ScienceDirect

Engineering Structures

journal homepage: www.elsevier.com/locate/engstruct

# Multiphase layout optimization for fiber reinforced composites considering a damage model

Junji Kato [a,*], Ekkehard Ramm [b]

[a] Mechanics of Materials Laboratory, Tohoku University, Aramaki-Aoba 6-6-06, Aoba, Sendai 980-8579, Japan
[b] Institute of Structural Mechanics, University of Stuttgart, Pfaffenwaldring 7, D-70550 Stuttgart, Germany

ARTICLE INFO

*Article history:*
Received 30 October 2011
Revised 29 October 2012
Accepted 31 October 2012

*Keywords:*
Material optimization
Fiber reinforced composites
Fiber reinforced concrete
Damage

ABSTRACT

The present study addresses an optimization strategy for fiber reinforced composites, specifically Fiber Reinforced Concrete (FRC) with a complex failure mechanism resulting from material brittleness of both matrix and fibers and also from the nonlinear interfacial behavior between those constituents. A prominent objective for this kind of composite is the improvement of ductility. The entire structural response of this material strongly depends on three factors, (i) material layout of fiber on a small scale, (ii) fiber geometry on the macroscopic structural level, and (iii) material parameters of interface between matrix and fiber.

The purpose of the present study is to improve the structural ductility of FRC by applying optimization; in the formulation not only the optimal material layout of fibers on the small scale but also the global fiber geometry are determined simultaneously. The proposed method is achieved by combining multiphase material optimization and material shape optimization, separately introduced by Kato et al. [11] and Kato and Ramm [12], respectively.

For the optimization problem a gradient-based optimization scheme is assumed. A method of moving asymptotes (MMA) is applied because of its numerically high efficiency and robustness. The performance of the proposed method is demonstrated by a series of numerical examples and compared with pure material shape optimization. It is verified that the proposed method gives more efficient results than the individual material shape optimization and that the structural ductility can be substantially improved.



## 1. Introduction

### 1.1. Overview

Nowadays textile fiber reinforced composites play a significant role in design of advanced materials and structures, such as Fiber Reinforced Polymers (FRP), Fiber Reinforced Metal (FRM), and Fiber Reinforced Glass (FRG). The present study addresses a promising composite material, namely Fiber Reinforced Concrete (FRC), sometimes also called textile reinforced concrete. FRC consists of fine grained concrete or mortar matrix and textile fiber mesh with a relatively low fiber content making it economically attractive [7]. Mostly glass or carbon fibers are used. Unlike conventional steel reinforcement this kind of textile fiber is corrosion free due to its high alkali-proof; this property allows for the manufacturing of light-weight thin-walled composite structures, see Fig. 1. However the critical aspect of this composite is that the structural response of FRC may result in brittle failure due to material brittleness of both concrete and fiber in addition to complex interfacial behavior between the constituents. The failure mechanism of FRC is highly complex, e.g. influenced by matrix cracking, slip of filaments in a roving, debonding of fibers from matrix and breaking of fibers, see Schladitz et al. [27]. The specific characteristic of FRC is an ideal target for optimization applying the overall structural ductility as objective which ought to be maximized for a prescribed fiber volume. In this context the 'structural ductility' means 'energy absorption capacity' which is measured by the internal energy summed over the entire structure up to a prescribed displacement of a dominant control point. For this objective it is of course not sufficient to base the optimization process on a linear material model, so that it is mandatory to consider material nonlinearities.

The structural response of FRC strongly depends on the following parameters: fiber size, fiber length, fiber location/orientation, impregnation, surface roughness of fiber, and the kind of fiber material itself, see Kato et al. [9].

Kato et al. [11] introduce a *multiphase material optimization* to improve the ductility of FRC with respect to fiber size, length and the combination of different fiber materials. This approach is considered as a material distribution problem derived from

* Corresponding author. Tel.: +81 22 795 7425; fax: +81 22 795 7423.
*E-mail address:* jkato@civil.tohoku.ac.jp (J. Kato).

0141-0296/$ - see front matter © 2012 Elsevier Ltd. All rights reserved.
http://dx.doi.org/10.1016/j.engstruct.2012.10.029

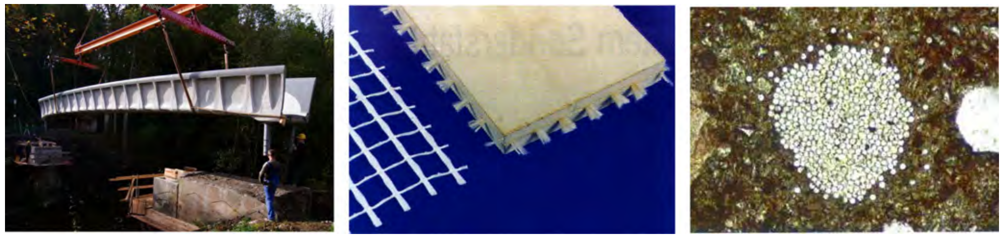

**Fig. 1.** FRC pedestrian bridge [5], FRC thin plate and textile fiber mesh [4], textile fiber in concrete matrix [8].

conventional topology optimization using a fixed finite element mesh, see Fig. 2. However it may encounter problems caused by the specific modeling of fiber reinforced composites. The thickness of fibers is in general very small and constant along the fiber length; this requires 'fine' discretization and provides a strict limitation in the discretization process.

In view of this problem a conventional 'smeared-type element concept' assuming an anisotropic material seems to be reasonable as used in, for example, Stegmann and Lund [29] and Stolpe and Stegmann [30]. However smeared-type elements are not sufficient for the present study because this approach concentrates more or less on the fiber orientation defined at each finite element and has less flexibility to deal with other design parameters mentioned above. Furthermore this approach results in fibers which are discontinuous between adjacent elements, and do not reflect realistic structural behavior especially for nonlinear response.

Therefore Kato and Ramm [12] propose an optimization methodology, denoted *material shape optimization*, to improve the structural ductility of FRC with respect to the 'fiber geometry' which is *independent* of the fixed finite element mesh. This approach allows to represent 'continuous long' fibers by applying the so-called embedded finite element formulation, see Fig. 3. However it is shown in Kato and Ramm [12] that this scheme does not always exploit all fibers; it is caused by a local minimum typical for non-convex optimization problems, see Fig. 4a. Consequently, this demand motivates the development of a new class of material optimization providing even more efficient optimal designs.

The purpose of the present study is to improve the structural ductility of FRC by developing a more flexible and efficient material optimization strategy. This approach is achieved by combining above two optimization schemes, i.e. multiphase material and material shape optimization. Therefore not only optimal fiber geometry at the global level but also fiber size and kinds of fiber materials are determined simultaneously, see Fig. 4b. In the present paper this combined strategy is denoted *multiphase layout optimization*.

For the material modeling a gradient-enhanced damage formulation [24–26] is applied for both concrete and fibers, and a discrete bond model [13–15,33] is used for the interface between the constituents. In the model we apply the embedded reinforcement element including the bond–slip kinematical relation by Balakrishnan and Murray [1]; for the two-dimensional model a

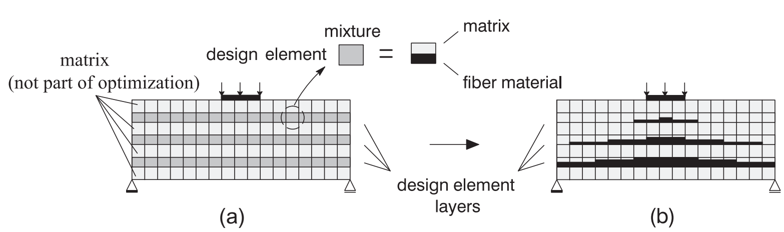


**Fig. 2.** Concept of multiphase material optimization, (a) initial and (b) optimized structures.

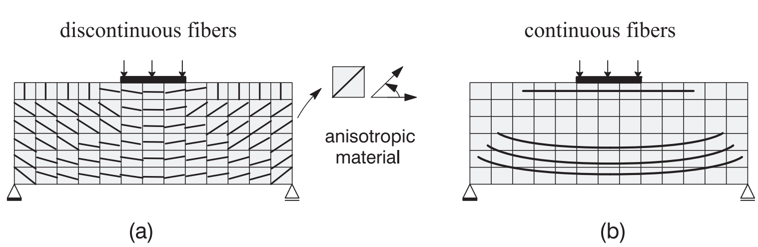


**Fig. 3.** Concept of material shape optimization, (a) conventional smeared-type element approach for fiber orientation and (b) material shape optimization.

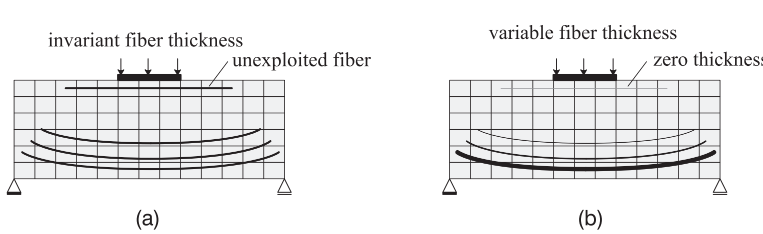


**Fig. 4.** Concept of multiphase layout optimization, (a) material shape optimization and (b) multiphase layout optimization.

curved fiber geometry is allowed which is defined globally by Bézier-splines.

The optimization problem is solved by a gradient-based optimization scheme. The method of moving asymptotes (MMA), see Svanberg [31], is used because it provides relatively reliable optimum solutions even for complex optimization problems. For the sensitivity analysis a variational semi-analytical direct method is used.

In the present paper several variables and functions are introduced which are already introduced in Kato and Ramm [12]. For the sake of compactness and avoiding duplication with [12], several symbols are listed in Appendix A.

## 2. Applied material models

### 2.1. Material model for constituents concrete and fiber

The nonlinear material behavior of both concrete and fiber is described by an isotropic continuum damage model. Firstly an equivalent strain measure is defined. For the concrete matrix de Vree's definition [32] of equivalent strains $\varepsilon_v^c$ is adopted as follows:

$$\varepsilon_v^c(I_1,J_2) = \frac{k-1}{2k(1-2v)}I_1 + \frac{1}{2k}\sqrt{\frac{(k-1)^2}{(1-2v)^2}I_1^2 - \frac{12k}{(1+v)^2}J_2}, \tag{1}$$

where $I_1$ denotes the first invariant of the strain tensor and $J_2$ the second invariant of the deviatoric strain tensor. $k$ indicates the ratio of compression relative to the tension strength and $v$ is Poisson's ratio. For the fiber we follow Mazars's definition [21] since the fiber is assumed to be a one-dimensional model

$$\varepsilon_v^f = \sqrt{\left\langle \varepsilon_L^f \right\rangle^2}, \tag{2}$$

where $\varepsilon_L^f$ is the fiber strain. For the damage evolution of both concrete and fiber we use an exponential damage law introduced by Mazars and Pijaudier-Cabot [21] as:

$$D(\kappa) = 1 - \frac{\kappa_0}{\kappa}(1 - \alpha + \alpha e^{-\beta(\kappa-\kappa_0)}) \quad \text{if } \kappa \geqslant \kappa_0, \tag{3}$$

where $D$ stands for the damage parameter ($0 \leqslant D \leqslant 1$) (Fig. 5a), $\alpha$ defines the final softening stage and $\beta$ governs the rate of damage growth. $\kappa_0$ is a threshold variable which determines damage initiation shown in Fig. 5b and $\kappa$ represents the most severe deformation the material has experienced during loading. In a conventional local damage model, $\kappa$ is related to the local equivalent strain $\varepsilon_v$ and the history variable $\kappa$ is defined by the Kuhn–Tucker relations, i.e. $\dot{\kappa} \geqslant 0,\ \varepsilon_v - \kappa \leqslant 0,\ \dot{\kappa}(\varepsilon_v - \kappa) = 0$. For non-local damage, $\kappa$ is related to a weighted volume average of the local equivalent strain $\varepsilon_v$, denoted as non-local equivalent strain $\tilde{\varepsilon}_v$. In the gradient-enhanced damage model [24–26], $\tilde{\varepsilon}_v$ is approximated implicitly as follows:

$$\tilde{\varepsilon}_v - c\nabla^2\tilde{\varepsilon}_v = \varepsilon_v, \tag{4}$$

$c$ is a positive parameter of dimension length squared regularizing the localization of the deformation. Thus in the Kuhn–Tucker equations $\varepsilon_v$ is replaced by the non-local equivalent strain $\tilde{\varepsilon}_v$ which is discretized in the finite element sense. Elastic unloading is included in the traditional way.

### 2.2. Material model for interface

The nonlinear interfacial behavior between fiber and matrix is expressed by a discrete bond model, see Krüger et al. [13]. This model was obtained by experiments using glass or carbon fibers and expresses a realistic interface response of FRC. The significant factors governing interfacial response are the bond strength and the debonding behavior. The influence of material properties at a small scale level and the stresses perpendicular to the fiber direction are included in the material formulation as important parameters. The bond stress–slip ($\sigma_L^i$–$u_L^i$) relation is expressed as:

$$\sigma_L^i = \tilde{u}^i \cdot \left\{ b + (1-b)\cdot\left(\frac{1}{1+(\tilde{u}^i)^{R_s}}\right)^{\frac{1}{R_s}} \right\} \cdot \sigma_0 \quad \text{for } u_L^i \leqslant u_1^i, \tag{5}$$

where $u_L^i$ is the slip length which will be introduced in Section 5. $\tilde{u}^i = u_L^i/u_0^i$ denotes the normalized slip. $u_0^i$ is a factor defined by the initial tangent $k_1$. $k_2$ is the tangent at slip $u_1^i$ where the bond stress achieves the maximum bond strength, see Fig. 5c. $b = k_2/k_1$ and $\sigma_0 = k_1 \cdot u_0^i$ are parameters to calculate the stresses and $R_s$ defines the radius of curvature at slip $u_1^i$. The stress–slip relation for the range $u_L^i > u_1^i$ is simply described by the adhesion strength $\sigma_m$ and the friction bond strength $\sigma_f$, see Fig. 5c

$$\sigma_m = \sigma_{m,0}\psi, \quad \sigma_f = \sigma_{f,0}\psi \tag{6}$$

with

$$\psi = 1 + \tanh\left[\alpha_r\frac{\sigma_R}{0.1f_c} - \alpha_f v\varepsilon_s\left(1 - \frac{r_s^2}{(r_s+h_s)^2}\right)^{-1}\right]. \tag{7}$$

Here $\psi$ denotes an additional parameter ($1 < \psi < 2$) which considers the influence of the kind of fiber material, the loading condition and the stresses perpendicular to a fiber direction. Further material parameters for the interface are listed in Appendix A. For a detailed description of this model it is referred to Krüger et al. [13–15]. In this model loading and unloading conditions are also considered.

This one-dimensional interface model is originally formulated for a fiber in a three-dimensional setting. If this model is utilized in a two-dimensional space as in this study, the interface has to be modified to hold the original total interface area.

## 3. Background: multiphase material and material shape optimization

### 3.1. Multiphase material optimization

This section introduces a two-phase material optimization applying the described damage formulation. The present methodology is

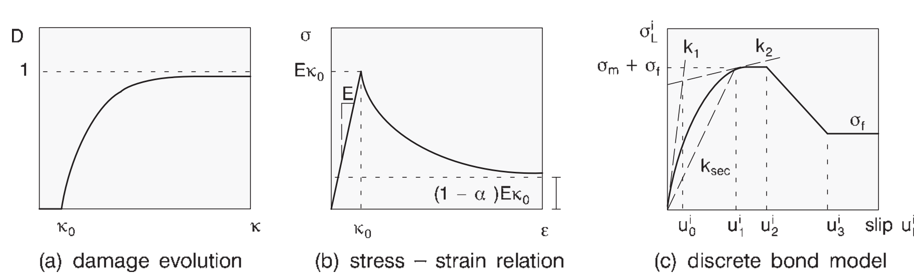


**Fig. 5.** (a) Exponential damage law and (b) corresponding uniaxial stress–strain response of damage model, (c) stress–strain relation of discrete bond model.

strongly related to topology optimization, in particular to the *Solid Isotropic Microstructure with Penalization of intermediate densities* for a one-phase material, the so-called SIMP approach [2,34], and to its generalization to multiphase topology optimization [28], for example used for composite structures. The development of these methods is briefly described in the sequel.

It is well known that the '0–1' integer topology optimization problem being a highly non-convex variational problem is ill-posed. In order to remedy this defect many material models providing a regularization have been developed. The SIMP method is the most popular model due to its numerical robustness.

In order to classify the present formulation within the multiphase optimization let us summarize the different concepts of material distribution problems (Fig. 6).

In the SIMP approach normalized density (porosity) $\rho_1/\rho_0$ $(0 \leqslant \rho_1/\rho_0 \leqslant 1)$ is taken as the design variable and the intermediate densities are used as mathematical vehicle to relax the ill-posed problem during optimization, see Fig. 6a. The exponent $\eta$ plays the role of a penalization factor without a physical meaning eventually leading to a pure or at least an almost pure 0–1 layout for a single material structure as depicted on the left side in the figure. The concept of topology optimization may also be applied to a single material for which intermediate densities physically exist, for example polymer or metal foams. Here the porosity, limited by upper and lower bounds, can be used as design parameter which varies in different regions of the structure; the effective modulus $\mathbb{C}_{\text{eff}}$ is often defined by a power-law formula, see for example Gibson and Ashby [6], Lipka [16], and Lipka and Ramm [17,18]. In this extended approach $\eta$ is a fitting variable rather than a penalization parameter, which guarantees the physically admissible intermediate stage.

The same concept for topology optimization can be utilized if two (or more) phases exist, i.e. when the void phase is replaced by a second solid material, see structure shown in Fig. 6b. Also in this multiphase version, intermediate stages in the sense of a physically existing smeared material on a small scale can be considered, indicated as a two-phase mixture in Fig. 6b right. In the present study this concept is applied in a slightly modified version. In fiber reinforced concrete straight or curved long fibers are embedded in the concrete matrix. As already indicated in Fig. 2a fixed finite element mesh is used. It is decomposed into a mesh for the matrix, not part of optimization, and a mesh for the design element layers. These contain two (or three) phases, namely concrete and fiber(s), which are combined to a material mixture. Within every layer either each individual element, a group of several finite elements or the entire layer is characterized by its own geometrical design parameter $s$.

$$s = r_1/r_0, \tag{8}$$

where $r_0$ and $r_1$ denote the height of a design element or the design element layer and that of phase-2 in the element or the layer, respectively. In this case the interpolation represents the material behavior of a real mixture, macroscopically describing the constitutive behavior of a material point or on a broader scale of a design element.

A function based on the volume fraction $r_1/r_0$ interpolates the material stiffness, i.e. the effective stiffness $\mathbb{C}_{\text{eff}}$ of the composite material between those of the two phases $\mathbb{C}_1$ and $\mathbb{C}_2$, see again Fig. 6b. More refined interpolations may be applied, derived from experiments or through homogenization.

The present study extends this *multiphase material optimization* to materially nonlinear problems applying the above described damage formulation with strain softening in order to consider a more realistic physical behavior of FRC. Since the applied damage formulation includes three extra material parameters, i.e. initial equivalent strain $\kappa_0$ and exponential softening parameters $\alpha$ and $\beta$ shown in Eq. (3), in addition to Young's modulus $E$ for each material, the interpolation of the mixture according to Fig. 6b is also applied to these additional parameters, namely

$$\zeta = (1 - s^{\hat{\eta}})\zeta_1 + s^{\hat{\eta}}\zeta_2, \tag{9}$$

where $\zeta$ represents either one of the four material parameters described above. $\zeta_1$ and $\zeta_2$ stand for the material properties of phase-1 (e.g. concrete matrix) and phase-2 (e.g. fiber), respectively, and are fixed values.

A closer look shows that Eq. (9) is not always sufficient to express the interpolation for all damage parameters since they have their own characteristics. In order to understand the features of the individual material parameters its relation to the present objective $f$, the structural ductility, is considered.

The part of $f$ for a material point is the area below the stress–strain curve and increases if either Young's modulus $E$ or initial equivalent strain $\kappa_0$ increases under the condition that all other material parameters are kept constant, see Fig. 7a and b. On the other hand the ductility decreases if either one of the softening parameters $\alpha$ or $\beta$ increases, see Fig. 7c and d.

Keeping this behavior in mind one can define related interpolation rules. It is obvious that Eq. (9) is a reasonable interpolation for the stiffness, namely the effective Young's modulus if $E_1 \leqslant E_2$, see for example Bendsøe and Sigmund [3]. It is apparent that the stiffer phase-2 has a dominant influence on the mixture expressed by a larger gradient at $s = 1$ than at $s = 0$, see Fig. 6b. Since $\kappa_0$ has essentially the same tendency it makes sense to use the same interpolation Eq. (9) also for this parameter, provided $\kappa_{0_1} \leqslant \kappa_{0_2}$. The situation is reverse for both softening parameters $\alpha$ and $\beta$. Assuming again $\zeta_1 \leqslant \zeta_2$ phase-1 is the "leading" constituent requiring a larger gradient of the interpolation function at $s = 0$; therefore the power law has to be concave and is expressed by

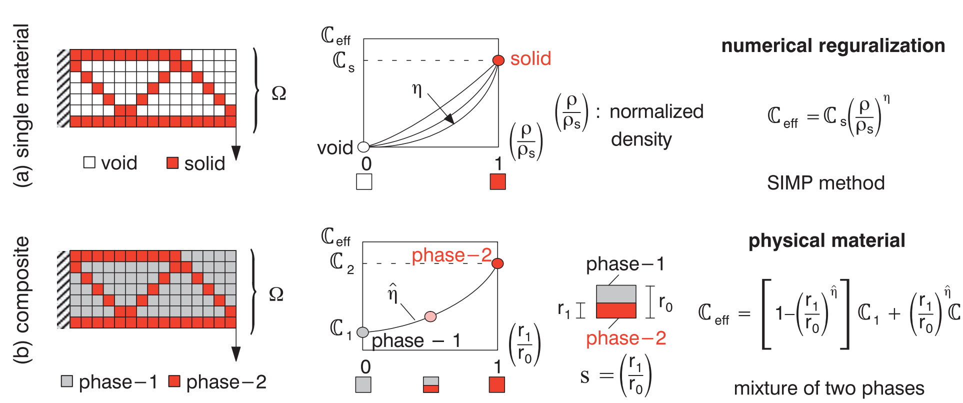


**Fig. 6.** Concept of multiphase material optimization (a) single material topology optimization with SIMP approach and (b) multiphase material optimization (two-phase).

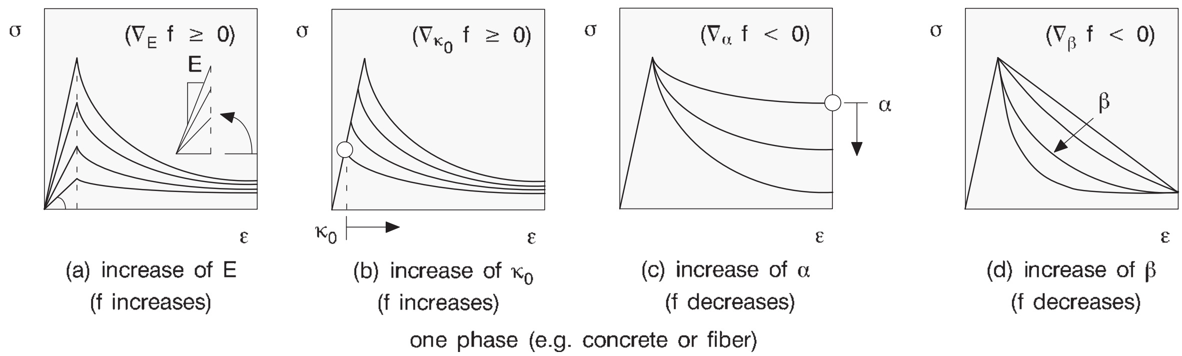


**Fig. 7.** Change of stress–strain relation of damage model with respect to one parameter increased under the condition that all other parameters are kept constant. (a) Young's modulus, $E$, (b) initial equivalent strain, $\kappa_0$, and (c) and (d) softening parameters, $\alpha$ and $\beta$.

$$\zeta = (1-s)^{\hat{\eta}}\zeta_1 + \left[1-(1-s)^{\hat{\eta}}\right]\zeta_2. \tag{10}$$

It may happen that for either of the four parameter $\zeta_1 > \zeta_2$. In this case the interpolation functions (9) and (10) have to be interchanged. Let us summarize the interpolation rules:

$$\zeta = \begin{cases} (1-s^{\hat{\eta}})\zeta_1 + s^{\hat{\eta}}\zeta_2 & \text{for } \zeta : \begin{cases} E, \quad \kappa_0 \quad (\zeta_1 \leqslant \zeta_2) \\ \text{or} \\ \alpha, \quad \beta \quad (\zeta_1 > \zeta_2) \end{cases} \\ (1-s)^{\hat{\eta}}\zeta_1 + [1-(1-s)^{\hat{\eta}}]\zeta_2 & \text{for } \zeta : \begin{cases} E, \quad \kappa_0 \quad (\zeta_1 > \zeta_2) \\ \text{or} \\ \alpha, \quad \beta \quad (\zeta_1 \leqslant \zeta_2) \end{cases} \end{cases} \tag{11}$$

Note that it is not necessarily required that the same value of the fitting parameter $\hat{\eta}$ is used for all four parameters. The detailed description including the extension to a three-phase composite is referred to Kato [10], Kato et al. [11].

### 3.2. Material shape optimization

The geometry of a continuous long fiber is defined in the global coordinate system. Hooks of textile fibers are not used. Due to this characteristic the layout of textile fibers in FRC can be rather simple, often parallel fibers or a mesh of straight fibers are used, see Fig. 1. Curved fibers are advantageous if an optimal structural response is looked for.

In this study the fiber geometry is defined globally by Bézier-splines. A quadratic Bézier-spline and its mathematical formulation are introduced in Fig. 8, where $\mathbf{r}$ stands for a position vector of the spline; $\vartheta$ $(0 \leqslant \vartheta \leqslant 1)$ is the local coordinate system of the spline. $p_j$ indicates the $j$th control point.

The fiber is embedded in the structure and the control points of the splines are moved in order to obtain the optimal fiber layout. The entire domain of the structure is defined in a parametric space $s$ $(0 \leqslant s \leqslant 1)$, see Fig. 8. Thus the normalized coordinates of control points are taken as the design variables defining the global fiber geometry in the physical space. The $j$th position vector of control point $p_j$ can be expressed as follows:

$$\mathbf{r}_j\left(s_j^x, s_j^y\right) = O(\hat{x}, \hat{y}) + \left(s_j^x L_x, s_j^y L_y\right), \tag{12}$$

where $O$ stands for the coordinate origin of the structure; $\hat{x}$, $\hat{y}$ are the corresponding global coordinates of $O$. $L$ denotes the contour lengths of the structure and the scripts $x, y$ on $L$ as well as $\mathbf{s}$ indicate the direction. Inserting Eq. (12) into the general mathematical formulation of Bézier-splines leads to the geometric definition of a fiber including the design variables $\hat{\mathbf{s}}$ as follows:

$$\mathbf{r}(\vartheta, s^x, s^y) = \sum_{j=0}^{n_b} \Phi_j(\vartheta)\mathbf{r}_j\left(s_j^x, s_j^y\right) \quad \text{with } \Phi_j = \frac{n_b!}{(n_b-j)!j!}\vartheta^j(1-\vartheta)^{n_b-j}, \tag{13}$$

where $n_b$ is the order of the Bézier-spline. Note that the coefficients $\Phi$ are independent of the design variables $\hat{\mathbf{s}}$.

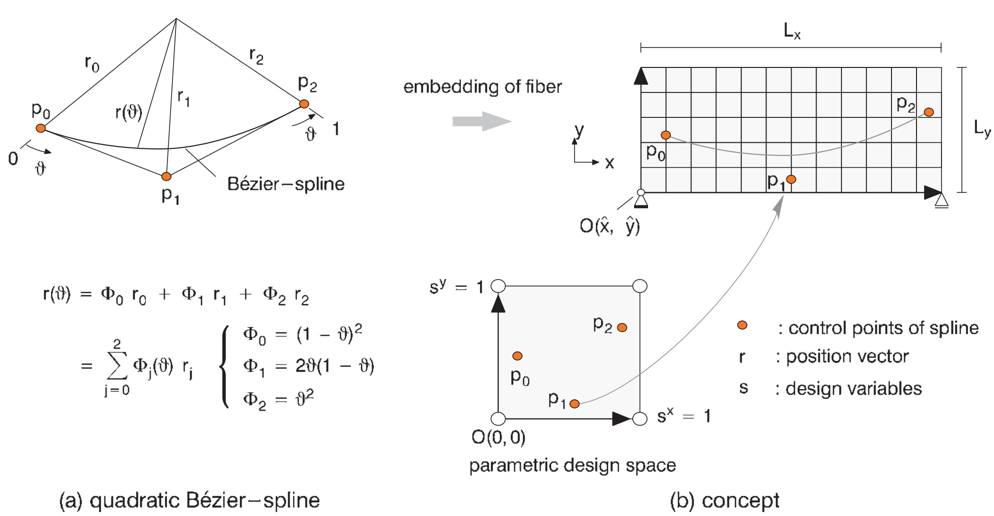


**Fig. 8.** (a) Quadratic Bézier-spline and (b) concept of global layout of fiber geometry.

Once the fiber geometry is defined by Eq. (13) the global coordinates for intersections of fibers and mesh are determined in order to establish the stiffness matrix and afterwards the internal forces of embedded fiber elements. This procedure is detailed in Kato and Ramm [12]. For further processing of the fiber mechanics the curved fiber in one finite element is for simplicity approximated by a straight line leading to a polygonal layout as indicated in Fig. 10.

## 4. Multiphase layout optimization

### 4.1. Basic concept

Multiphase layout optimization is formulated by combining multiphase material optimization and material shape optimization. Fig. 9 describes the notation of the design variables for two- and three-phase fibers based on the embedded reinforcement formulation. For the two-phase fiber, phase-1 indicates 'no material' and phase-2 is 'fiber material'. For the three-phase fiber, phase-1, -2, and -3 stand for no material, fiber 1, and fiber 2, respectively. In the latter case a fiber consists of two different fiber materials.

In multiphase material optimization the prescribed constant fiber thickness $r_0$ is defined as the thickness of a design element in the fixed FE-mesh (Figs. 2 and 6) while in this study $r_0$ is the prescribed maximum thickness of an embedded fiber with a geometry independent of the fixed FE-mesh. In the two-phase fiber $r_1$ is the thickness of the 'fiber' while in the three-phase fiber $r_1$ describes the total fiber thickness of fiber 1 and fiber 2 and $r_2$ is the thickness of fiber 2. The fiber thicknesses $r_1$, $r_2$ can vary during optimization but are assumed to be constant along the entire fiber length in space.

The design variables $\hat{\mathbf{s}}$ consist of the two kinds of variables $\hat{\mathbf{s}}_r$ and $\hat{\mathbf{s}}_g$. For convenience $\hat{\mathbf{s}}_r$ are called 'material design variables' and $\hat{\mathbf{s}}_g$ 'shape design variables', respectively. As can be seen in Fig. 9, the concept of volume fraction is applied for the material design variable, i.e. $s_r = r_1/r_0$ for the two-phase fiber, $s_{r_1} = r_1/r_0$ and $s_{r_2} = r_2/r_1$ for the three-phase fiber. $s_r$ and $s_{r_1}$ control the effective material parameters between 'no-material' and 'fiber(s)' and $s_{r_2}$ describes the effective material parameters of 'mixture' between fiber 1 and fiber 2 ($0 \leqslant s_r, s_{r_1}, s_{r_2} \leqslant 1$). The fiber fills with 'no-material' if $s_r = 0$ or $s_{r_1} = 0$. This situation means that the fiber has no mechanical property and does not influence the structural response although the geometry of the fiber still remains. This 'no-material' fiber does not provide any 'defect' of volume of the concrete matrix because fibers are simply superimposed on the concrete matrix in the embedded reinforcement formulation.

The shape design variables $\hat{\mathbf{s}}_g$ are identical to those of material shape optimization, which stand for the normalized coordinates of control points of the global fiber geometry. $l_f$ in Fig. 9 is the length of a single fiber within an embedded reinforcement element and depends indirectly on the shape design variables $\hat{\mathbf{s}}_g$.

In the sequel the effective material parameters are discussed considering the characteristics of material design variables.

### 4.2. Two-phase fiber

The chosen embedded two-phase fiber may contain layers with 'no material'. This is different from the two-phase material of multiphase material optimization in which both phases are assumed to be solid materials.

Considering this difference, it is of course possible to interpret the present two-phase fiber as a 'single material fiber' using fiber thickness $r_1$ as material design variable $s_r$. If one applies the two-phase interpolation rules Eq. (11) for the effective material parameters by inserting 'zero' to all material properties of phase-1, i.e. $\zeta_1 = 0$, with a linear interpolation factor $\hat{\eta} = 1$ the effective material parameter $\zeta$ for the two-phase fiber is reduced from Eq. (11) to

$$\zeta = s_r \zeta_2, \tag{14}$$

where $\zeta_2$ stands for all four material properties of phase-2 as introduced in Section 3.1, i.e. $E_2$, $\kappa_{02}$, $\alpha_2$, and $\beta_2$. Both procedures provide fundamentally the same structural properties. For instance, the element stiffness matrix of an embedded fiber can be reformulated considering Eq. (85) in Kato and Ramm [12] as follows:

$$\mathbf{K}_e^f = \int_{\Omega_\xi^f} \mathbf{B}^{f^T} \underbrace{\mathbb{C}_{\text{eff}}^f}_{=s_r \mathbb{C}_2^f} \mathbf{B}^f \underbrace{|\mathbf{J}^f|}_{=r_0 l_f} d\Omega_\xi^f \tag{15}$$

$$= \int_{\Omega_\xi^f} \mathbf{B}^{f^T} \mathbb{C}_2^f \mathbf{B}^f \underbrace{|\mathbf{J}^f|}_{=r_1 l_f} d\Omega_\xi^f, \tag{16}$$

where some subscripts have been eliminated from Eq. (85) of Kato and Ramm [12] for simplicity. $\mathbb{C}_{\text{eff}}^f$ is the matrix of the effective elasto-damage secant material stiffness for the two-phase fiber and $\mathbb{C}_2^f$

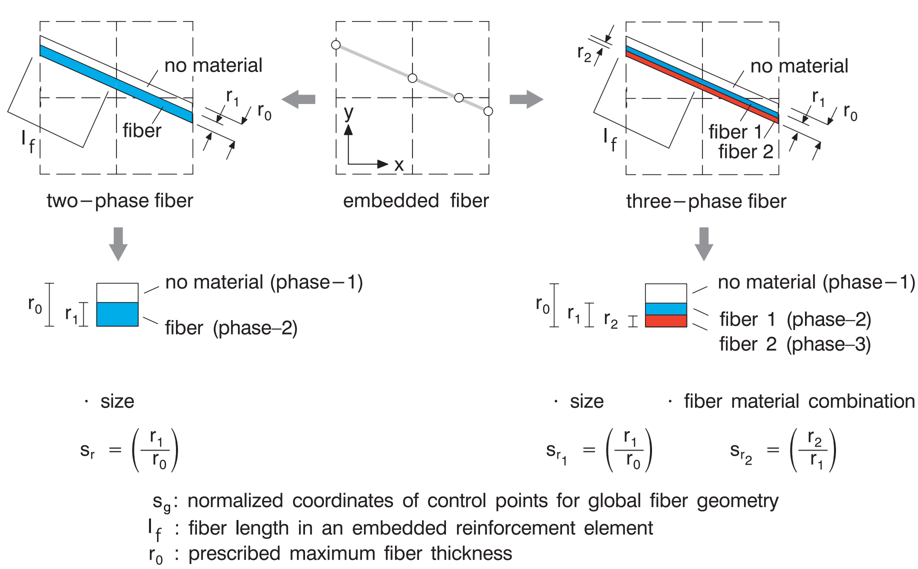


**Fig. 9.** Concept of present approach and notation of design variables.

is that of the individual fiber (phase-2). Eq. (15) indicates the expression using the two-phase interpolation rule Eq. (14) while Eq. (16) expresses the simplified formulation, in which $|\mathbf{J}^f|$ absorbs the design variable $s_r$ or $r_1$ instead of $\mathbb{C}^f_{\mathrm{eff}}$.

Consequently, this two-phase fiber is simply transformed to the single material of phase-2 with real fiber thickness $r_1$ which varies during optimization depending on the design variable $s_r$. The determinant of Jacobian $|\mathbf{J}^f|$ represents the real fiber volume of an embedded fiber and depends on both $s_g$ and $s_r$. This transformation considerably reduces the derivation process of sensitivities for the 'material design' part because all terms in Eq. (16) except $|\mathbf{J}^f|$ do not depend on the material design variable $s_r$.

### 4.3. Three-phase fiber

The concept of the three-phase fiber follows that of the two-phase fiber. Inserting $\zeta_1 = 0$ and $\hat{\eta} = 1$ into the interpolation rule between phase-1 (no material) and the mixture ($\zeta_{23}$) of phase-2 and -3 in Eq. (15) of Kato et al. [11] and rearranging the formulation yields the following reduced expression:

$$\zeta = \begin{cases} s_{r_1}\left\{\underbrace{\left(1 - s_{r_2}^{\hat{\eta}}\right)\zeta_2 + s_{r_2}^{\hat{\eta}}\zeta_3}_{\zeta_{23}}\right\} & \text{for } \zeta : \begin{cases} E, & \kappa_0 \ (\zeta_2 \leqslant \zeta_3) \\ \text{or} & \\ \alpha, & \beta \ (\zeta_2 > \zeta_3) \end{cases} \\ s_{r_1}\left\{\underbrace{(1 - s_{r_2})^{\hat{\eta}}\zeta_2 + \left[1 - (1 - s_{r_2})^{\hat{\eta}}\right]\zeta_3}_{\zeta_{23}}\right\} & \text{for } \zeta : \begin{cases} E, & \kappa_0 \ (\zeta_2 > \zeta_3) \\ \text{or} & \\ \alpha, & \beta \ (\zeta_2 \leqslant \zeta_3) \end{cases} \end{cases} \tag{17}$$

$$\varphi = \begin{cases} s_{r_1}\left\{\underbrace{\left(1 - s_{r_2}^{\hat{\eta}}\right)\varphi_2 + s_{r_2}^{\hat{\eta}}\varphi_3}_{\varphi_{23}}\right\} & \text{for} \begin{cases} \text{all except } \nu & (\varphi_2 \leqslant \varphi_3) \\ \text{or} & \\ \nu & (\varphi_2 > \varphi_3) \end{cases} \\ s_{r_1}\left\{\underbrace{(1 - s_{r_2})^{\hat{\eta}}\varphi_2 + [1 - (1 - s_{r_2})^{\hat{\eta}}]\varphi_3}_{\varphi_{23}}\right\} & \text{for} \begin{cases} \text{all except } \nu & (\varphi_2 > \varphi_3) \\ \text{or} & \\ \nu & (\varphi_2 \leqslant \varphi_3) \end{cases} \end{cases} \tag{21}$$

where $\zeta_{23}$ indicates the effective material parameter of phase-2 and phase-3 as well. The fitting parameter $\hat{\eta} \neq 1$ in Eq. (17) is introduced for the interpolation between phase-2 and phase-3; it is not necessarily required that the same value of $\hat{\eta}$ is used for all four parameters as mentioned in Section 3.1.

Similarly, the system of element stiffness matrix of the three-phase fiber is expressed as:

$$\mathbf{K}^f_e = \int_{\Omega^f_\xi} \mathbf{B}^{f^T} \underbrace{\mathbb{C}^f_{\mathrm{eff}}}_{=s_{r_1}\mathbb{C}^f_{23}} \mathbf{B}^f \underbrace{|\mathbf{J}^f|}_{=r_0 l_f} d\Omega^f_\xi \tag{18}$$

$$= \int_{\Omega^f_\xi} \mathbf{B}^{f^T} \mathbb{C}^f_{23} \mathbf{B}^f \underbrace{|\mathbf{J}^f|}_{=r_1 l_f} d\Omega^f_\xi, \tag{19}$$

where $\mathbb{C}^f_{\mathrm{eff}}$ stands for the effective elasto-damage secant material stiffness of the three-phase fiber and $\mathbb{C}^f_{23}$ is that of two-phase fiber consisting of phase-2 and phase-3. $\mathbb{C}^f_{23}$ is controlled by the second material design variable $s_{r_2}$. In this case $s_{r_1}$ is included into the determinant of Jacobian matrix $|\mathbf{J}^f|$. Thus $|\mathbf{J}^f|$ in the three-phase fiber depends not only on the shape design variable $s_g$ but also on the material variable $s_r$ as for the two-phase fiber.

Incidentally we describe the concept of three-phase fiber in this section considering its potential idea as demonstrated by Kato et al. [11] although no numerical example for it is shown in the present paper. In our preliminary numerical examples for the three-phase fiber using AR-glass (alkali resistance glass) and carbon, the proposed algorithm itself shows good performance as we expect, however it gets inaccurate sensitivity when sudden failure of the structure (steep strain softening) is allowed. This is an other problem to that we care and a typical problem resulting from the rigid body rotation introduced by Olhoff and Rasmussen [22] or Olhoff et al. [23] when a variational semi-analytical approach is utilized in sensitivity analysis. Taking this situation into account, we describe the basic concept and formulations of the three-phase fiber in this section.

### 4.4. Interpolation rule for interface

The interpolation rule for the interface follows the previous section. According to Eq. (14) the effective interfacial parameter $\varphi$ for the two-phase fiber can be written as:

$$\varphi = s_r \varphi_2, \tag{20}$$

where $\varphi$ stands for all interfacial material parameters relevant to fiber materials introduced in Section 2.2, i.e. $\sigma_{m,0}, \sigma_{f,0}, k_1, k_2, k_{\mathrm{sec}}, u^i_2, u^i_3, h_s, R_s$ and $\nu$. $\varphi_2$ represents the material properties of phase-2. Note that other data mentioned in Section 2.2, i.e. the compression strength of concrete $f_c$, the coefficients $\alpha_r$ and $\alpha_f$, are constants and independent of the volume fraction of fiber materials. This interpolation rule indicates that if the material design variable $s_r$ is zero, i.e. 'no material', the mechanical response of interface vanishes simultaneously.

Analogously, the effective interfacial parameter $\varphi$ for the three-phase fiber is assumed as follows:

(21)

where $\varphi_2$ and $\varphi_3$ indicate the interfacial material properties of phase-2 (fiber 1) and phase-3 (fiber 2), respectively. All effective interfacial parameters $\varphi$ except for Poisson's ratio $\nu$ have a similar characteristic as $E$ and $\kappa_0$ in Eq. (17) while $\nu$ follows the behavior of $\alpha$ and $\beta$. Up to now very little is known about this 'mixture' of interfaces. Thus physically reliable fitting parameters $\hat{\eta}$ for each effective parameter need to be investigated by experiments or homogenization.

Again the determinant of Jacobian matrix for interface $|\mathbf{J}^i|$ depends on the shape design variable $s_g$ as well as on the material design variable $s_r$.

## 5. Embedded reinforcement element

### 5.1. Kinematical assumption for interface between concrete and fiber

The embedded reinforcement element (Fig. 10a) applied in this study considers a bond–slip relation between concrete and fiber. We introduce the kinematical relation of the interface based on the assumption by Balakrishnan and Murray [1]. In the kinematical assumption the slip at an arbitrary point is considered as the relative displacement between concrete and fiber measured along the

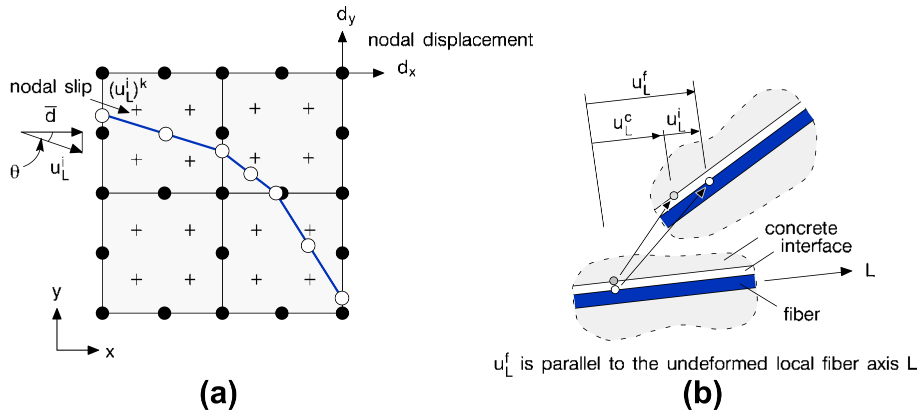


**Fig. 10.** (a) Embedded reinforcement element patch and (b) notion for displacements of slip.

axis of the fiber. The components of the displacements can be written as:

$$u_L^f = u_L^c + u_L^i, \tag{22}$$

where $u_L^i$ is the slip length or relative displacement introduced in Eq. (5). $u_L^f$ and $u_L^c$ are the displacements of fiber and concrete at the considered point, respectively, see Fig. 10b. The slip values of the originally curved fiber at the intersection of two adjacent elements have to be equal; this is not the case for the polygonal geometry assumed above. In order to satisfy the compatibility at least in an average sense the slip length $u_L^i$ is projected onto the global $x$-axis

$$\bar{d} = \cos\theta \cdot u_L^i \rightarrow u_L^i = \bar{t}\bar{d} \quad \text{with } \bar{t} = (\cos\theta)^{-1}, \tag{23}$$

where $\theta$ is the angle between fiber axis and $x$-axis, see Fig. 10. Thus the compatibility of the slip-length is enforced for $\bar{d}$. From $u_L^i$ the local bond strain $\varepsilon_L^i$ is obtained which in turn leads to the local fiber strain $\varepsilon_L^f$

$$\varepsilon_L^f = \underbrace{\varepsilon_L^c}_{\mathbf{T}_1^\varepsilon \boldsymbol{\varepsilon}_G^c} + \varepsilon_L^i. \tag{24}$$

Matrix $\mathbf{T}^\varepsilon$ transforms the global strain $\boldsymbol{\varepsilon}_G$ of a two-dimensional continuum into the local one $\boldsymbol{\varepsilon}_L$ under plane stress condition, see Appendix A in Kato and Ramm [12]. $\mathbf{T}_1^\varepsilon$ represents the first row of $\mathbf{T}^\varepsilon$ extracting the local strain $\varepsilon_L^c$ in fiber direction from the global concrete strain $\boldsymbol{\varepsilon}_G^c$.

## 6. Finite element formulation of FRC

### 6.1. Discretized principle virtual work

Since the present study applies a gradient enhanced damage model for both concrete and fibers and uses a nonlinear interface model between fiber and matrix, the virtual work $\delta W$ is decomposed into

$$\delta W = \delta W_{\text{int}} - \delta W_{\text{ext}} = \delta W_{\text{int}}^c + \delta W_{\text{int}}^f + \delta W_{\text{int}}^i - \delta W_{\text{ext}} = 0, \tag{25}$$

where $\delta W_{\text{int}}^c$, $\delta W_{\text{int}}^f$, and $\delta W_{\text{int}}^i$ stand for the internal virtual work of concrete, fibers and interfaces, respectively, and $\delta W_{\text{ext}}$ denotes the external virtual work. The lengthy derivation of each virtual work expression and all formulations are shifted to Kato and Ramm [12].

The virtual work expressions in Section 5.1 of [12] contain three independent variables, namely the displacement field in the concrete element $\mathbf{u}$, the non-local equivalent strain $\tilde{\varepsilon}_v$ and the slip length $u_L^i$ which are discretized in the finite element sense. In the present study a two-dimensional eight-node quadratic plane stress element is applied for the concrete matrix. The non-local strain is discretized by bilinear shape functions within this element. Note that the interface slip is discretized as a three-node quadratic one-dimensional element ($n_i = 3$), whereas the non-local strain enhancement of the fibers is only linearly interpolated based on the two values at the fiber beginning and end obtained from the non-local strain values in the concrete element

$$\mathbf{u} = \sum_{k=1}^{n_c} N_k d^k \quad \text{or} \quad \mathbf{u} = \mathbf{N}\mathbf{d}, \tag{26}$$

$$\tilde{\varepsilon}_v = \sum_{k=1}^{n_e} \tilde{N}_k e^k \quad \text{or} \quad \tilde{\varepsilon}_v = \tilde{\mathbf{N}}\mathbf{e}, \tag{27}$$

$$u_L^i = \sum_{k=1}^{n_i} N_k^i (u_L^i)^k = \sum_{k=1}^{n_i} N_k^i (\bar{t}\bar{d})^k = \sum_{k=1}^{n_i} \bar{N}_k \bar{d}^k \quad \text{or} \quad u_L^i = \bar{\mathbf{N}}\bar{\mathbf{d}}, \tag{28}$$

where $\mathbf{d}$ is a vector with eight nodal displacements, $\mathbf{e}$ with four nodal values and $\bar{\mathbf{d}}$ contains three nodal slip values.

The three nodal values of the projected slip lengths are summed in the vector $\bar{\mathbf{d}}$

$$\bar{\mathbf{d}} = [\bar{d}^1 \quad \bar{d}^2 \quad \bar{d}^3]^T. \tag{29}$$

$\bar{\mathbf{N}}$ contains the shape function for the interface defined in the global coordinate system. Analogously the local bond strain $\varepsilon_L^i$ of Eq. (24) in one element can be expressed as:

$$\varepsilon_L^i = \sum_{k=1}^{n_i} B_k^i (\bar{t}\bar{d})^k = \bar{t}\mathbf{B}^i\bar{\mathbf{d}} = \bar{\mathbf{B}}\bar{\mathbf{d}}, \tag{30}$$

where $\mathbf{B}^i$ and $\bar{\mathbf{B}}$ stand for $B$-operator matrices for the interface defined in local and global coordinate systems, respectively. The local fiber strain $\varepsilon_L^f$ can be written according to Eq. (24)

$$\varepsilon_L^f = \mathbf{T}_1^\varepsilon \boldsymbol{\varepsilon}_G^c + \varepsilon_L^i = \mathbf{T}_1^\varepsilon \mathbf{B}^f \mathbf{d} + \bar{\mathbf{B}}\bar{\mathbf{d}}. \tag{31}$$

Introducing Eqs. (26),(27),(28),(30) and (31) into the virtual work expressions at the actual time $t+1$ leads to

$$\begin{aligned} \delta W_u &= \delta W_{u,\text{int}}^c + \delta W_{u,\text{int}}^f - \delta W_{\text{ext}} \quad \forall\ \delta\mathbf{d} \\ &= \bigcup_{e=1}^{n_{\text{ele}}} \delta\mathbf{d}^T \left[ \underbrace{\int_{\Omega^c} \mathbf{B}^{c^T} \boldsymbol{\sigma}^c d\Omega^c}_{\mathbf{f}_{\text{int},u}^c} + \underbrace{\int_{\Omega^f} \mathbf{B}^{f^T} (\mathbf{T}_1^\varepsilon)^T \sigma_L^f \, d\Omega^f}_{\mathbf{f}_{\text{int},u}^f} - \underbrace{\lambda_{t+1} \int_\Gamma \mathbf{N}^{c^T} \mathbf{t}_0 \, d\Gamma}_{\mathbf{f}_{\text{ext}}} \right] \\ &= 0 \end{aligned} \tag{32}$$

$$
\begin{aligned}
\delta W_e &= \delta W_e^c + \delta W_e^f \quad \forall\ \delta \mathbf{e} \\
&= \bigcup_{e=1}^{n_{\text{ele}}^c} \delta \mathbf{e}^T \left[ \underbrace{\int_{\Omega^c} (\widetilde{\mathbf{B}}^c)^T \boldsymbol{\tau}^c d\Omega^c + \int_{\Omega^c} (\widetilde{\mathbf{N}}^c)^T \left(\tilde{\varepsilon}_v^c - \varepsilon_v^c\right) d\Omega^c}_{\mathbf{f}_{\text{int},e}^c} \right] \\
&+ \bigcup_{e=1}^{n_{\text{ele}}^f} \delta \mathbf{e}^T \left[ \underbrace{\int_{\Omega^f} (\widetilde{\mathbf{B}}^f)^T \left(\mathbf{T}_1^d\right)^T \tau_L^f d\Omega^f + \int_{\Omega^f} (\widetilde{\mathbf{N}}^f)^T \left(\tilde{\varepsilon}_{v,L}^f - \varepsilon_{v,L}^f\right) d\Omega^f}_{\mathbf{f}_{\text{int},e}^f} \right] = 0
\end{aligned}
\tag{33}
$$

$$
\delta W_{\text{int}}^i = \bigcup_{e=1}^{n_{\text{ele}}^i} \delta \bar{\mathbf{d}}^T \left[ \underbrace{\int_{\Omega^f} \overline{\mathbf{B}}^T \sigma_L^f\, d\Omega^f + \int_{\Omega^i} \overline{\mathbf{N}}^T \sigma_L^i\, d\Omega^i}_{\mathbf{f}_{\text{int},i}^i} \right] = 0 \quad \forall\ \delta \bar{\mathbf{d}}, \tag{34}
$$

where 'time' $t$ simply means the 'loading step number' for a nonlinear static problem.

$\mathbf{B}^c$ is the usual kinematic operator matrix; $\widetilde{\mathbf{B}}^c$ is derived from the gradient of the non-local equivalent strain

$$\nabla \tilde{\varepsilon}_v^c = \widetilde{\mathbf{B}}^c \mathbf{e}, \tag{35}$$

and $\widetilde{\mathbf{B}}^f$ that of the corresponding part in the fiber

$$\nabla \tilde{\varepsilon}_{v,L}^f = \mathbf{T}_1^d \nabla \tilde{\boldsymbol{\varepsilon}}_{v,G}^f = \mathbf{T}_1^d \widetilde{\mathbf{B}}^f \mathbf{e}, \tag{36}$$

where $\mathbf{T}_1^d$ is the first row of a rotation matrix $\mathbf{T}^d$. $\lambda$ inserted in Eq. (32) denotes the load factor with respect to a reference traction load $\mathbf{t}_0$.

### 6.2. Element matrices

Introducing damage and interface models into the virtual work expressions and linearizing with respect to the primary variables $\mathbf{d}$, $\mathbf{e}$ and $\bar{\mathbf{d}}$ leads after assembly to the stiffness expression

$$
\underbrace{\begin{bmatrix} \mathbf{K}_{\text{dd}}^{c+f} & \mathbf{K}_{\text{de}}^{c+f} & \mathbf{K}_{\text{d}\bar{d}}^{f} \\ \mathbf{K}_{\text{ed}}^{c+f} & \mathbf{K}_{\text{ee}}^{c+f} & 0 \\ \mathbf{K}_{\bar{d}d}^{f} & 0 & \mathbf{K}_{\bar{d}\bar{d}}^{i} \end{bmatrix}^n}_{\mathbf{K}_T}
\underbrace{\begin{bmatrix} \Delta \mathbf{d} \\ \Delta \mathbf{e} \\ \Delta \bar{\mathbf{d}} \end{bmatrix}^{n+1}}_{\Delta \mathbf{u}}
= - \underbrace{\begin{bmatrix} \mathbf{f}_{\text{int},u}^c + \mathbf{f}_{\text{int},u}^f - \mathbf{f}_{\text{ext}} \\ \mathbf{f}_{\text{int},e}^c + \mathbf{f}_{\text{int},e}^f \\ \mathbf{f}_{\text{int},i}^i \end{bmatrix}^n}_{\mathbf{R}}, \tag{37}
$$

where $\mathbf{K}_T$, $\Delta\mathbf{u}$ and $\mathbf{R}$ are the tangential stiffness matrix, the incremental displacement/strain vector and the residual force vector, respectively. The superscripts $n$ and $n + 1$ on the matrix and vectors indicate the iteration number in the increment. For the derivation of the corresponding stiffness matrices in $\mathbf{K}_T$ and the forces in $\mathbf{R}$ it is referred to Appendices in Kato and Ramm [12].

## 7. Structural optimization of FRC

### 7.1. Optimization problem

In general an optimization problem is defined by an objective $f(\hat{\mathbf{s}})$, equality constraints $\mathbf{h}(\hat{\mathbf{s}})$ and inequality constraints $\mathbf{g}(\hat{\mathbf{s}})$. In this study the objective is to maximize the structural ductility for a prescribed fiber volume. As the ductility is defined by the internal energy summed up over the entire structure with a prescribed nodal displacement $\hat{d}_j$ [19,20], the mathematical formulation of the optimization problem of FRC can be written as follows:

$$
\text{minimize } f(\hat{\mathbf{s}}) = -\left[ \int_{\Omega^c} \int_{\hat{\varepsilon}^c} \boldsymbol{\sigma}^c d\boldsymbol{\varepsilon}^c\, d\Omega^c + \int_{\Omega^f} \int_{\hat{\varepsilon}_L^f} \sigma_L^f d\varepsilon_L^f\, d\Omega^f + \int_{\Omega^i} \int_{\hat{u}_L^i} \sigma_L^i du_L^i\, d\Omega^i \right] \tag{38}
$$

$$
\text{subject to } \mathrm{g}(\hat{\mathbf{s}}) = \bigcup_{e=1}^{n_{\text{ele}}^f} \int_{\Omega_\xi^f} \underbrace{|\mathbf{J}^f|}_{r_1\ l_f}\, d\Omega_\xi^f - \hat{\mathrm{V}} \leqslant 0 \tag{39}
$$

$$\hat{\mathbf{s}}_L \leqslant \hat{\mathbf{s}}_{r_i} \leqslant \hat{\mathbf{s}}_U \quad i = 1, \ldots, n_{s_r} \tag{40}$$

$$\hat{\mathbf{s}}_L \leqslant \hat{\mathbf{s}}_{g_i} \leqslant \hat{\mathbf{s}}_U \quad i = 1, \ldots, n_{s_g} \tag{41}$$

$$\hat{\mathbf{s}} = \hat{\mathbf{s}}_r \cup \hat{\mathbf{s}}_g \tag{42}$$

where $\widehat{V}$ denotes the prescribed fiber volume. $n_{s_r}$ denotes the number of the design variables for $\hat{\mathbf{s}}_r$ and $n_{s_g}$ for $\hat{\mathbf{s}}_g$, respectively.

### 7.2. Equilibrium conditions and total derivative of design function

The sensitivities of the design functions (objective, constraints, etc.) depend on the gradients of the state variables $\mathbf{u}(\mathbf{d}, \mathbf{e}, \bar{\mathbf{d}})$. These are derived from the three equilibrium conditions (15), (17), and (21) in [12] at time $t + 1$.

The total derivative of the design functions with respect to the design variables can be decomposed into an explicit and an implicit part. As indicated the design functions depend on the structural response which in turn is implicitly related to the optimization variables, for example the objective $f = f(\mathbf{s}, \mathbf{u}(\mathbf{d}, \mathbf{e}, \bar{\mathbf{d}}))$. This leads to

$$
\begin{aligned}
\nabla_s(\bullet) &= \nabla_s^{\text{ex}}(\bullet) + \nabla_u(\bullet)\nabla_s \mathbf{u} \\
&= \nabla_s^{\text{ex}}(\bullet) + \nabla_d(\bullet)\nabla_s \mathbf{d} + \nabla_e(\bullet)\nabla_s \mathbf{e} + \nabla_{\bar{d}}(\bullet)\nabla_s \bar{\mathbf{d}},
\end{aligned}
\tag{43}
$$

In this case the derivatives of the constraint tend to become highly nonlinear with respect to the design variables because different classes of design variables are involved. For this the method of moving asymptotes based on Svanberg [31] is applied to solve the present optimization problem.

## 8. Sensitivity analysis

### 8.1. Overview of sensitivity analysis

The main effort of sensitivity analysis is the calculation of implicit part $\nabla_s \mathbf{u}$. For a direct sensitivity analysis this part is obtained by exploiting the stiffness expression containing the tangent stiffness matrix and the so-called pseudo load vector, see Eq. (68). This pseudo load vector is obtained through the derivatives of the equilibrium conditions, (15), (17), and (21) in [12] with respect to the design variables and by assembling the individual pseudo load vectors for each equilibrium condition. For this the gradients of constitutive equations and also the explicit part of the derivative of objective function are described first in the next two sections.

In this section the derivation of sensitivity with respect to the material design variable $\hat{s}_r$ is described; the sensitivity with respect to shape design variable $\hat{s}_g$ is given in [12].

### 8.2. Gradients of constitutive equations

This section introduces the gradients of constitutive equation with respect to the material design variable $\hat{s}_r$.

Firstly, the derivatives of the strains, displacements, local and non-local equivalent strains with respect to the material design variable $\hat{s}_r$ are discussed. These derivatives are compiled in [12]; all explicit terms of Eqs. (37), (39)–(41) and (43)–(48) in the reference vanish for the case of material design variables because the 'geometrical' functions $\mathbf{N}^{c/f}$, $\mathbf{B}^{c/f}$, $\widetilde{\mathbf{N}}^{c/f}$, $\widetilde{\mathbf{B}}^{c/f}$, $\overline{\mathbf{N}}$, $\overline{\mathbf{B}}$, $\mathbf{T}_1^d$, and $\mathbf{T}_1^{\varepsilon}$ do not depend on the material design variables.

The main variables of the damage models for concrete, fibers and interface depend on the material design variable $\hat{\mathbf{s}}_r$ in the following way:

$$\boldsymbol{\sigma} = \boldsymbol{\sigma}(D,\ \mathbb{C}(E(\hat{\mathbf{s}}_r),\ \nu(\hat{\mathbf{s}}_r)),\ \boldsymbol{\varepsilon}(\hat{\mathbf{s}}_r)), \tag{44}$$

$$D = D(\kappa,\ \kappa_0(\hat{\mathbf{s}}_r),\ \alpha(\hat{\mathbf{s}}_r),\ \beta(\hat{\mathbf{s}}_r)), \tag{45}$$

$$\kappa = \kappa(\tilde{\varepsilon}_v(\mathbf{e}(\hat{\mathbf{s}}_r)),\ \kappa_u(\mathbf{e}_u(\hat{\mathbf{s}}_r))), \tag{46}$$

$$\sigma^i_L = \sigma^i_L\big(u^i_L(\hat{\mathbf{s}}_r),\ u^i_{L_u}(\hat{\mathbf{s}}_r),\ \varphi(\hat{\mathbf{s}}_r)\big). \tag{47}$$

Eqs. (44)–(46) cover both concrete and fibers. Here $\kappa_u$, $\mathbf{e}_u$, and $u^i_{L_u}$ denote history variable, nodal non-local strain vector, and slip length at the time $t_u$, respectively, when unloading starts.

Utilizing the above equations the stress derivatives of concrete matrix $\nabla_s\boldsymbol{\sigma}^c$, fiber $\nabla_s\sigma^f_L$, and interface $\nabla_s\sigma^i_L$ with respect to a material design variable $\hat{s}_r$ at time $t+1$ are introduced as follows:

$$\begin{aligned}\nabla_s\boldsymbol{\sigma}^c &= \frac{\partial\boldsymbol{\sigma}^c}{\partial\boldsymbol{\varepsilon}^c}\frac{\partial\boldsymbol{\varepsilon}^c}{\partial s} + \frac{\partial\boldsymbol{\sigma}^c}{\partial\tilde{\varepsilon}^c_v}\frac{\partial\tilde{\varepsilon}^c_v}{\partial s} + \frac{\partial\boldsymbol{\sigma}^c}{\partial\kappa^c_u}\frac{\partial\kappa^c_u}{\partial s}\\ &= \mathbb{C}^c_{\mathrm{ed}}\nabla^{\mathrm{im}}_s\boldsymbol{\varepsilon}^c + \bar{\mathbf{E}}^c\nabla^{\mathrm{im}}_s\tilde{\varepsilon}^c_v + \underbrace{\breve{\mathbf{E}}^c\nabla_s\kappa^c_u}_{explicit},\end{aligned} \tag{48}$$

$$\begin{aligned}\nabla_s\sigma^f_L &= \frac{\partial\sigma^f_L}{\partial\varepsilon^f_L}\frac{\partial\varepsilon^f_L}{\partial s} + \frac{\partial\sigma^f_L}{\partial\tilde{\varepsilon}^f_{v,L}}\frac{\partial\tilde{\varepsilon}^f_{v,L}}{\partial s} + \frac{\partial\sigma^f_L}{\partial\kappa^f_u}\frac{\partial\kappa^f_u}{\partial s} + \frac{\partial\sigma^f_L}{\partial D^f}\frac{\partial D^f}{\partial s} + \frac{\partial\sigma^f_L}{\partial\mathbb{C}^f_{\mathrm{el},L}}\frac{\partial\mathbb{C}^f_{\mathrm{el},L}}{\partial s}\\ &= \mathbb{C}^f_{\mathrm{ed},L}\nabla^{\mathrm{im}}_s\varepsilon^f_L + \bar{\mathbf{E}}^f\nabla^{\mathrm{im}}_s\tilde{\varepsilon}^f_{v,L} + \underbrace{\breve{\mathbf{E}}^f\nabla_s\kappa^f_u + \mathbf{G}^f}_{explicit},\end{aligned} \tag{49}$$

$$\begin{aligned}\nabla_s\sigma^i_L &= \frac{\partial\sigma^i_L}{\partial u^i_L}\frac{\partial u^i_L}{\partial s} + \frac{\partial\sigma^i_L}{\partial u^i_{L_u}}\frac{\partial u^i_{L_u}}{\partial s} + \frac{\partial\sigma^i_L}{\partial\varphi}\frac{\partial\varphi}{\partial s}\\ &= k_L\nabla^{\mathrm{im}}_s u^i_L + \underbrace{k_{L_u}\nabla_s u^i_{L_u} + \mathbf{G}^i}_{explicit},\end{aligned} \tag{50}$$

with the abbreviations

$$\mathbf{G}^f \equiv \frac{\partial\sigma^f_L}{\partial D^f}\left(\frac{\partial D^f}{\partial\kappa^f_0}\frac{\partial\kappa^f_0}{\partial s} + \frac{\partial D^f}{\partial\alpha^f}\frac{\partial\alpha^f}{\partial s} + \frac{\partial D^f}{\partial\beta^f}\frac{\partial\beta^f}{\partial s}\right) + \frac{\partial\sigma^f_L}{\partial\mathbb{C}^f_{\mathrm{el},L}}\left(\frac{\partial\mathbb{C}^f_{\mathrm{el},L}}{\partial E^f}\frac{\partial E^f}{\partial s} + \frac{\partial\mathbb{C}^f_{\mathrm{el},L}}{\partial\nu^f}\frac{\partial\nu^f}{\partial s}\right), \tag{51}$$

$$\mathbf{G}^i \equiv \frac{\partial\sigma^i_L}{\partial\varphi}\frac{\partial\varphi}{\partial s}, \tag{52}$$

where $s$ describes the material design variable $\hat{s}_r$. $\mathbf{G}^f$ and $\mathbf{G}^i$ denote the explicit parts of stress derivative for fibers and interface, respectively, relevant to a mixture of phase-2 and -3.

Thus these terms vanish if the 'two-phase fiber' (no-material and one fiber) is used. If the three-phase fiber is adopted, the elasto-damage secant material tensor $\mathbb{C}^f_{\mathrm{ed},L}$ needs to be replaced by the 'effective' elasto-damage secant material tensor $\left(\mathbb{C}^f_{\mathrm{ed},L}\right)_{23}$; it is obtained by an interpolation between those of phase-2 and -3.

Further abbreviations are

$$\bar{\mathbf{E}}^c \equiv \frac{\partial\boldsymbol{\sigma}^c}{\partial\tilde{\varepsilon}^c_v} \quad \text{and} \quad \bar{\mathbf{E}}^f \equiv \frac{\partial\sigma^f_L}{\partial\tilde{\varepsilon}^f_{v,L}}. \tag{53}$$

$\bar{\mathbf{E}}^{c/f}$ are detailed in Eqs. (80)/(89) in [12]. $\mathbb{C}^{c/f}_{\mathrm{ed}}$ is the elasto-damage secant material tensor, see Eq. (83) in [12].

The last abbreviations are terms relevant to 'un-/reloading',

$$\breve{\mathbf{E}}^c \equiv \frac{\partial\boldsymbol{\sigma}^c}{\partial\kappa^c_u} = \frac{\partial\boldsymbol{\sigma}^c}{\partial D^c}\frac{\partial D^c}{\partial\kappa^c}\frac{\partial\kappa^c}{\partial\kappa^c_u} \quad \text{and} \quad \breve{\mathbf{E}}^f \equiv \frac{\partial\sigma^f_L}{\partial\kappa^f_u} = \frac{\partial\sigma^f_L}{\partial D^f}\frac{\partial D^f}{\partial\kappa^f}\frac{\partial\kappa^f}{\partial\kappa^f_u} \tag{54}$$

with

$$\frac{\partial\kappa^{c/f}}{\partial\kappa^{c/f}_u} = \begin{cases}0 & \text{if loading}\\ 1 & \text{if un-/reloading.}\end{cases} \tag{55}$$

$\bar{\mathbf{E}}^{c/f}$ are relevant to 'loading' and are non-zero; $\breve{\mathbf{E}}^{c/f}$ vanish under loading. On the contrary $\bar{\mathbf{E}}^{c/f}$ become zero and $\breve{\mathbf{E}}^{c/f}$ are non-zero for un-/reloading. The remaining terms in Eq. (54) are $\nabla_\kappa D^{c/f}$, which are calculated by following Eq. (3). The derivatives $\nabla_s\kappa^{c/f}_u$ in Eqs. (48) and (49) and $\nabla_s u^i_{L_u}$ in Eq. (50) are obtained in terms of Eqs. (44) and (47) and Eq. (41) in [12], respectively,

$$\nabla_s\kappa^c_u = \widetilde{\mathbf{N}}^c\nabla_s\mathbf{e}_u, \quad \nabla_s\kappa^f_u = \widetilde{\mathbf{N}}^f\nabla_s\mathbf{e}_u, \tag{56}$$

$$\nabla_s u^i_{L_u} = \overline{\mathbf{N}}\nabla_s\bar{\mathbf{d}}_u, \tag{57}$$

where $\bar{\mathbf{d}}_u$ is the nodal slip length at the time $t_u$. Note that $\mathbf{e}_u$ and $\bar{\mathbf{d}}_u$ need to be updated whenever 'loading' occurs. $k_L$ in Eq. (50) denotes the tangent modulus of the interface which is explicitly obtained from Eq. (5) and Fig. 5c introducing the given material properties. $k_{L_u}$ is the tangent modulus of the interface at the time $t_u$.

### 8.3. Sensitivity for explicit term of objective function

The explicit part of sensitivity of the objective function is expressed as follows:

$$\nabla^{\mathrm{ex}}_s f = \nabla^{\mathrm{ex}}_s(f^c + f^f + f^i) \tag{58}$$

with

$$\nabla^{\mathrm{ex}}_s f^c = -\int_{\Omega^c}\int_{\hat{\boldsymbol{\varepsilon}}^c}\nabla^{\mathrm{ex}}_s(\boldsymbol{\sigma}^c)d\boldsymbol{\varepsilon}^c\,d\Omega^c, \tag{59}$$

$$\begin{aligned}\nabla^{\mathrm{ex}}_s f^f = &-\int_{\Omega^f}\int_{\hat{\varepsilon}^f_L}\left(\nabla^{\mathrm{ex}}_s\left(\sigma^f_L\right)d\varepsilon^f_L + \sigma^f_L\nabla^{\mathrm{ex}}_s d\varepsilon^f_L\right)d\Omega^f\\ &-\int_{\Omega^f_\xi}\int_{\hat{\varepsilon}^f_L}\sigma^f_L d\varepsilon^f_L\nabla_s|\mathbf{J}^f|d\Omega^f_\xi,\end{aligned} \tag{60}$$

$$\begin{aligned}\nabla^{\mathrm{ex}}_s f^i = &-\int_{\Omega^i}\int_{\hat{u}^i_L}\left(\nabla^{\mathrm{ex}}_s(\sigma^i_L)du^i_L + \sigma^i_L\nabla^{\mathrm{ex}}_s du^i_L\right)d\Omega^i\\ &-\int_{\Omega^i_\xi}\int_{\hat{u}^i_L}\sigma^i_L du^i_L\nabla_s|\mathbf{J}^i|d\Omega^i_\xi.\end{aligned} \tag{61}$$

The second terms in Eqs. (60) and (61) are integrated in the parametric space $\xi$.

Most often $\nabla^{\mathrm{ex}}_s f^c$ is zero because the functions for concrete, e.g. shape functions and $B$-operators, are independent of the design variables as mentioned above. Thus the explicit parts of all derivatives for the concrete matrix vanish. $\nabla^{\mathrm{ex}}_s f^c$ becomes non-zero only when unloading starts at a concrete element in which damage has already been initiated, see the last term of Eq. (48).

The determinants of Jacobian matrices $|\mathbf{J}^f|$ and $|\mathbf{J}^i|$ for fiber and interface elements map the parametric element domains onto their real space. The stress derivatives $\nabla^{\mathrm{ex}}_s\sigma^f_L$ and $\nabla^{\mathrm{ex}}_s\sigma^i_L$ are the explicit parts of Eqs. (49) and (50), respectively.

In the following sections the implicit part of sensitivity of the objective function is discussed.

### 8.4. Calculation of sensitivity coefficients

The derivative of the first equilibrium condition Eq. (16) in [12] with respect to a design variable $\hat{s}_r$ is obtained considering Eq. (32). As mentioned the 'geometrical' functions do not depend on a 'material' design variable $\hat{s}_r$. Thus the terms which contain the derivative of the geometrical functions vanish:

$$\begin{aligned}&\int_{\Omega^c}\mathbf{B}^{c^T}\nabla_s(\boldsymbol{\sigma}^c)d\Omega^c + \int_{\Omega^f}\mathbf{B}^{f^T}(\mathbf{T}^\varepsilon_1)^T\nabla_s\left(\sigma^f_L\right)d\Omega^f\\ &+\int_{\Omega^f_\xi}\mathbf{B}^{f^T}(\mathbf{T}^\varepsilon_1)^T\sigma^f_L\nabla_s|\mathbf{J}^f|d\Omega^f_\xi - \nabla_s\lambda_{t+1}\underbrace{\int_{\Gamma_\xi}\mathbf{N}^{c^T}\mathbf{t}_0|\widetilde{\mathbf{J}}|d\Gamma_\xi}_{\mathbf{P}} = 0.\end{aligned} \tag{62}$$

Substituting Eqs. (48) and (49) into Eq. (62) results in

$$\mathbf{K}^{c}_{dd}\nabla_s\mathbf{d}+\mathbf{K}^{f}_{dd}\nabla_s\mathbf{d}+\mathbf{K}^{f}_{d\bar{d}}\nabla_s\bar{\mathbf{d}}+\mathbf{K}^{c}_{de}\nabla_s\mathbf{e}+\mathbf{K}^{f}_{de}\nabla_s\mathbf{e}$$
$$=\nabla_s\lambda_{t+1}\mathbf{P}-\widetilde{\mathbf{P}}^{d}_{5}-\widetilde{\mathbf{P}}^{d}_{6}-\widetilde{\mathbf{P}}^{d}_{7}-\underbrace{\int_{\Omega^f}\mathbf{B}^{f^T}(\mathbf{T}^{\varepsilon}_{1})^{T}\mathbf{G}^{f}\,d\Omega^{f}}_{\widetilde{\mathbf{P}}^{d}_{8}}, \tag{63}$$

where all stiffness matrices, the load vector $\mathbf{P}$, and the pseudo load vectors $\widetilde{\mathbf{P}}^{d}_{5}$ to $\widetilde{\mathbf{P}}^{d}_{7}$ in Eq. (63) are common to those of material shape optimization. For these formulas and also for the pseudo load vectors for the second and third equilibrium equations mentioned below it is referred to [12]. $\widetilde{\mathbf{P}}^{d}_{8}$ denotes an additional pseudo load vector which vanishes if the two-phase fiber is applied.

Analogously the derivative of the second equilibrium condition Eq. (17) in [12] with respect to a design variable $\hat{s}_r$ is obtained considering Eq. (33). Deleting the terms which include the derivative of the geometrical functions and inserting Eqs. (43)–(48) from [12] into the obtained derivative of the equilibrium condition Eq. (17) in [12] yields

$$\mathbf{K}^{c}_{ee}\nabla_s\mathbf{e}-\mathbf{K}^{c}_{ed}\nabla_s\mathbf{d}+\mathbf{K}^{f}_{ee}\nabla_s\mathbf{e}+\mathbf{K}^{f}_{ed}\nabla_s\mathbf{d}=-\widetilde{\mathbf{P}}^{e}_{3}. \tag{64}$$

All stiffness matrices and $\widetilde{\mathbf{P}}^{e}_{3}$ in Eq. (64) are common to those of material shape optimization.

Similarly the derivative of the third equilibrium condition Eq. (20) in [12] is obtained considering Eq. (34)

$$\int_{\Omega^f}\overline{\mathbf{B}}^{T}\nabla_s\sigma^{f}_{L}\,d\Omega^{f}+\int_{\Omega^f_\xi}\overline{\mathbf{B}}^{T}\sigma^{f}_{L}\nabla_s|\mathbf{J}^{f}|\,d\Omega^{f}_{\xi}+\int_{\Omega^i}\overline{\mathbf{N}}^{T}\nabla_s\sigma^{i}_{L}\,d\Omega^{i}$$
$$+\int_{\Omega^i_\xi}\overline{\mathbf{N}}^{T}\sigma^{i}_{L}\nabla_s|\mathbf{J}^{i}|\,d\Omega^{i}_{\xi}=0. \tag{65}$$

The bond–slip relation Eq. (5) does not include any term related to the non-local equivalent strain, thus the non-local term is excluded from Eq. (49):

$$\nabla_s\sigma^{f}_{L}=\mathbb{C}^{f}_{ed,L}\nabla^{im}_{s}\varepsilon^{f}_{L}+\mathbf{G}^{f}. \tag{66}$$

Substituting Eqs. (50) and (66) into Eq. (65) yields:

$$\mathbf{K}^{i}_{\bar{d}\bar{d}}\nabla_s\bar{\mathbf{d}}+\mathbf{K}^{f}_{\bar{d}d}\nabla_s\mathbf{d}=-\widetilde{\mathbf{P}}^{\bar{d}}_{3}-\widetilde{\mathbf{P}}^{\bar{d}}_{6}-\widetilde{\mathbf{P}}^{\bar{d}}_{7}-\underbrace{\int_{\Omega^f}\overline{\mathbf{B}}^{T}\mathbf{G}^{f}\,d\Omega^{f}}_{\widetilde{\mathbf{P}}^{\bar{d}}_{8}}-\underbrace{\int_{\Omega^i}\overline{\mathbf{N}}^{T}\mathbf{G}^{i}\,d\Omega^{i}}_{\widetilde{\mathbf{P}}^{\bar{d}}_{9}}, \tag{67}$$

where the pseudo load vectors $\widetilde{\mathbf{P}}^{\bar{d}}_{3}$, $\widetilde{\mathbf{P}}^{\bar{d}}_{6}$ and $\widetilde{\mathbf{P}}^{\bar{d}}_{7}$ in Eq. (67) are equivalent to those of material shape optimization. $\widetilde{\mathbf{P}}^{\bar{d}}_{8}$ and $\widetilde{\mathbf{P}}^{\bar{d}}_{9}$ denote extra pseudo load vectors and vanish again if the two-phase fiber is applied.

*8.5. Total sensitivity*

Assembling Eqs. (63), (64) and (67) for multiphase material optimization and Eqs. (58), (59) and (63) from [12] for material shape optimization leads to the following compact matrix expression

$$\begin{bmatrix}\mathbf{K}^{c+f}_{dd} & \mathbf{K}^{c+f}_{de} & \mathbf{K}^{f}_{d\bar{d}}\\ \mathbf{K}^{c+f}_{ed} & \mathbf{K}^{c+f}_{ee} & 0\\ \mathbf{K}^{f}_{\bar{d}d} & 0 & \mathbf{K}^{i}_{\bar{d}\bar{d}}\end{bmatrix}\begin{bmatrix}\nabla_s\mathbf{d}\\ \nabla_s\mathbf{e}\\ \nabla_s\bar{\mathbf{d}}\end{bmatrix}=\nabla_s\lambda_{t+1}\begin{bmatrix}\mathbf{P}\\0\\0\end{bmatrix}-\underbrace{\begin{bmatrix}\sum_{l=1}^{4}\widetilde{\mathbf{P}}^{d}_{l}\\ \sum_{l=1}^{2}\widetilde{\mathbf{P}}^{e}_{l}\\ \sum_{l=1,l\neq3}^{5}\widetilde{\mathbf{P}}^{\bar{d}}_{l}\end{bmatrix}}_{\mathbf{P}_g}$$
$$-\underbrace{\begin{bmatrix}\sum_{l=5}^{7}\widetilde{\mathbf{P}}^{d}_{l}\\ \widetilde{\mathbf{P}}^{e}_{3}\\ \widetilde{\mathbf{P}}^{\bar{d}}_{3}+\widetilde{\mathbf{P}}^{\bar{d}}_{6}+\widetilde{\mathbf{P}}^{\bar{d}}_{7}\end{bmatrix}}_{\mathbf{P}_{g+r}}-\underbrace{\begin{bmatrix}\widetilde{\mathbf{P}}^{d}_{8}\\0\\ \sum_{l=8}^{9}\widetilde{\mathbf{P}}^{\bar{d}}_{l}\end{bmatrix}}_{\mathbf{P}_r}, \tag{68}$$

where $\mathbf{P}_g$, $\mathbf{P}_r$, and $\mathbf{P}_{g+r}$ denote the pseudo load vectors with respect to a shape design variable $\hat{s}_g$, a material design variable $\hat{s}_r$, and both $\hat{s}_g$ and $\hat{s}_r$, respectively. $\mathbf{P}_g$ is zero when the derivatives with respect to the material design variable $\hat{s}_r$ are calculated while $\mathbf{P}_r$ vanishes when the derivatives with respect to the shape design variable $\hat{s}_g$ are determined or when the two-phase fiber is applied. The common pseudo load vector $\mathbf{P}_{g+r}$ is relevant to the derivatives of the determinants of Jacobian $\nabla_s|\mathbf{J}^{f}|$ and $\nabla_s|\mathbf{J}^{i}|$ which depend on both, $\hat{s}_g$ and $\hat{s}_r$.

Eq. (68) has the format of the typical stiffness equation adding up all terms on the right hand side to a pseudo load vector $\mathbf{P}_{pse}$:

$$\mathbf{K}_T\nabla_s\hat{\mathbf{u}}=\mathbf{P}_{pse}=\nabla_s\lambda_{t+1}\hat{\mathbf{P}}+\widetilde{\mathbf{P}}_{pse}. \tag{69}$$

The tangential stiffness matrix is $\mathbf{K}_T$ is the same regardless of the selected design variables. Thus the present sensitivity analysis which includes two kinds of design variables is solved by switching only to the respective pseudo load vector depending on the selected design variables.

The next question is how to deal with the derivative of the load factor $\nabla_s\lambda$. Note that the derivatives based on a load-controlled algorithm differ from those based on a displacement-controlled scheme related to a certain nodal displacement 'component' $u_j=\hat{u}_j$ of the structure for the optimization of ductility [19,20]. A load-controlled algorithm renders $\nabla_s\lambda = 0$ while for a displacement controlled algorithm the sensitivity of the nodal displacement for the controlled degree of freedom $\hat{u}_j$ is equal to zero. For this case the sensitivity of the load factor is derived subsequently,

$$\nabla_s\hat{u}_j=\nabla_s\lambda_{t+1}\frac{\breve{u}_j}{\lambda_{t+1}}+(\nabla_s\hat{u}_j)_{pse}=0, \tag{70}$$

where $\breve{u}_j$ and $(\nabla_s\hat{u}_j)_{pse}$ are the $j$th component of vectors $\breve{\mathbf{u}}$ and $(\nabla_s\hat{\mathbf{u}})_{pse}$ is expressed as:

$$\breve{\mathbf{u}}=\mathbf{K}_T^{-1}\lambda_{t+1}\widehat{\mathbf{P}}, \tag{71}$$
$$(\nabla_s\hat{\mathbf{u}})_{pse}=\mathbf{K}_T^{-1}\widetilde{\mathbf{P}}_{pse}. \tag{72}$$

Substituting $\breve{u}_j$ and $(\nabla_s\hat{u}_j)_{pse}$ into Eq. (70) yields

$$\nabla_s\lambda_{t+1}=-\frac{(\nabla_s\hat{u}_j)_{pse}}{\breve{u}_j}\lambda_{t+1}. \tag{73}$$

According to the above equations the derivative of the total nodal displacement vector $\nabla_s\hat{\mathbf{u}}$ is calculated as follows:

$$\nabla_s\hat{\mathbf{u}}=\breve{\mathbf{u}}\frac{\nabla_s\lambda_{t+1}}{\lambda_{t+1}}+(\nabla_s\hat{\mathbf{u}})_{pse}. \tag{74}$$

Finally, the total sensitivity of the objective function can be obtained by inserting Eq. (74) into Eq. (43) and accumulating each sensitivity over the load increment step number $n_{step}$ as:

$$\nabla_s f=\sum_{t=1}^{n_{step}}\nabla_s f_t=\sum_{t=1}^{n_{step}}\left(\nabla^{ex}_{s}f_t+\nabla_u f_t^{T}\nabla_s\hat{\mathbf{u}}_t\right), \tag{75}$$

where $f_t$ indicates the ductility increment in the $t$th load increment.

## 9. Numerical examples

Firstly the results of material shape optimization and multiphase layout optimization are compared in terms of two FRC structures. Secondly an L-shaped plate of FRC is optimized in which not only horizontal but also vertical fibers are employed. For the properties of the interface for all examples it is referred to Kato [10].

One purpose of this section is to observe whether multiphase layout optimization could remedy the deficit of material shape optimization, namely how the 'unexploited fibers' can be avoided at the final optimization stage, providing additional ductility.

*9.1. Material shape optimization vs. multiphase layout optimization*

*9.1.1. Deep beam*

As the first numerical example the deep beam with four AR-glass fibers is chosen as depicted in Fig. 11b and the material properties are given in Fig. 11a. The beam was already investigated in [12] using carbon fibers which lead to a stiffer and more brittle behavior than AR-glass.

Due to symmetry only one half of the system is analyzed. Plane-stress conditions are assumed. The beam thickness is assumed to be only 1 mm, since no out-of-plane actions are considered. 200 eight-noded finite elements are used for concrete and 68 three-noded elements for the interface, respectively. The initial fiber thickness is set to 0.4 mm as shown in Fig. 11b; the fiber geometry is approximated by a symmetric biquadratic Bézier-spline, see Fig. 11c. Due to symmetry the locations of the control points $p_3$ and $p_4$ are coupled to $p_1$ and $p_0$, respectively. In addition the $y$-coordinate of $p_1$ is set equal to that of $p_2$, and the $x$-coordinate of $p_1$ is placed always at the center between the $x$-coordinates of $p_0$ and $p_2$. Thus the number of design variables for a single fiber geometry is three, i.e. $s_{g1}$, $s_{g2}$, and $s_{g3}$, see Fig. 11c, leading to a total number of 12. The initial set of the shape design variables is (i) $s_{g1} = 0.075$ (i.e. the $x$-coordinate of $p_0$ is $0.075 \times 400$ mm) for all fibers and (ii) $s_{g2}$ and $s_{g3}$ are assumed to be 0.15, 0.38, 0.62, and 0.85 for the four fibers. Taking into account that thick concrete covers for textile fibers are obsolete, we adopt the lower bound $s_L = 0.01$ and the upper one $s_U = 0.99$ for $s_{g2}$ and $s_{g3}$ of all fibers. For the design variable $s_{g1}$, the lower and upper bounds are set to $s_L = 0.01$ and $s_U = 0.4$, respectively.

The initial and maximum fiber thicknesses are set to $r_1 = 0.4$ mm and $r_0 = 0.8$ mm in multiphase layout optimization. Thus the initial set of the material design variables is $s_r = 0.5$ $(0 < s_r < 1)$ and the fiber thickness may vary within 0 mm $< r_1 <$ 0.8 mm. The lower and upper bounds for the material design variables $\mathbf{s}_r$ are defined as $s_L = 0.001$ and $s_U = 0.99$, respectively. For the semi-analytical sensitivity analysis a central finite difference scheme with $\Delta s = 1.0 \times 10^{-7}$ is adopted so that the perturbation does not violate both bounds. For the two-phase fiber, the fitting parameter can be set to $\hat{\eta} = 1$ as mentioned in Section 4.2.

The analysis is carried out with a displacement controlled method; the control point $c$ is at the lower center of the beam. The prescribed nodal displacement $\hat{u}$ ($-y$-direction) at the control point is 0.4mm, see Fig. 11b. The total fiber volume is 1.4% and is held constant for both cases during optimization. Optimization is continued until the change of the objective function value falls below $1.0 \times 10^{-8}$. The central finite difference scheme with finite perturbation $\Delta s = 1.0 \times 10^{-7}$ is also applied for the material design variables.

Fig. 12a is the result obtained by pure material shape optimization and Fig. 12b by two-phase layout optimization with a total

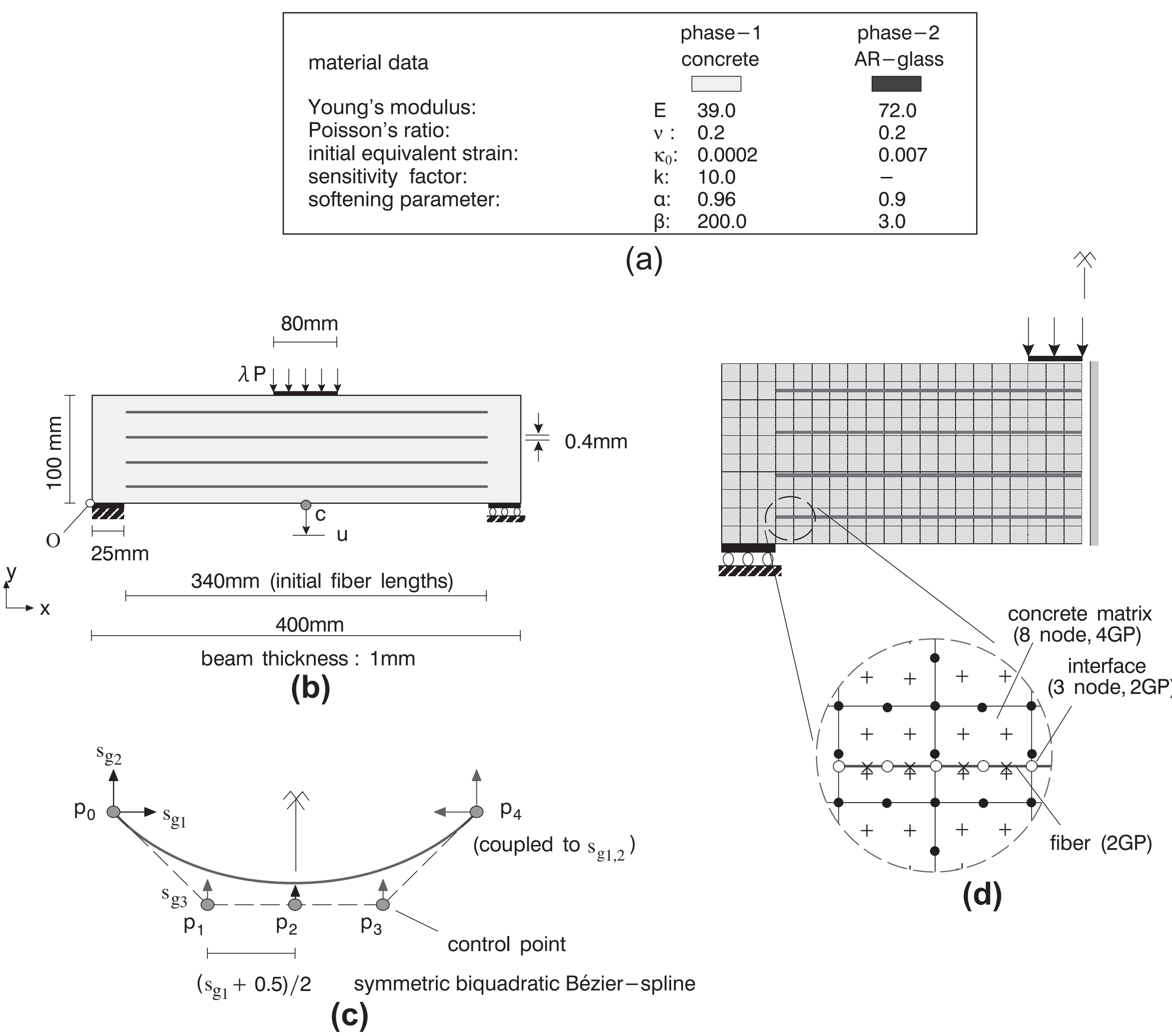


**Fig. 11.** Structural situation, (a) material properties, (b) structural model, (c) geometrical definition of fiber, and (d) FE mesh.

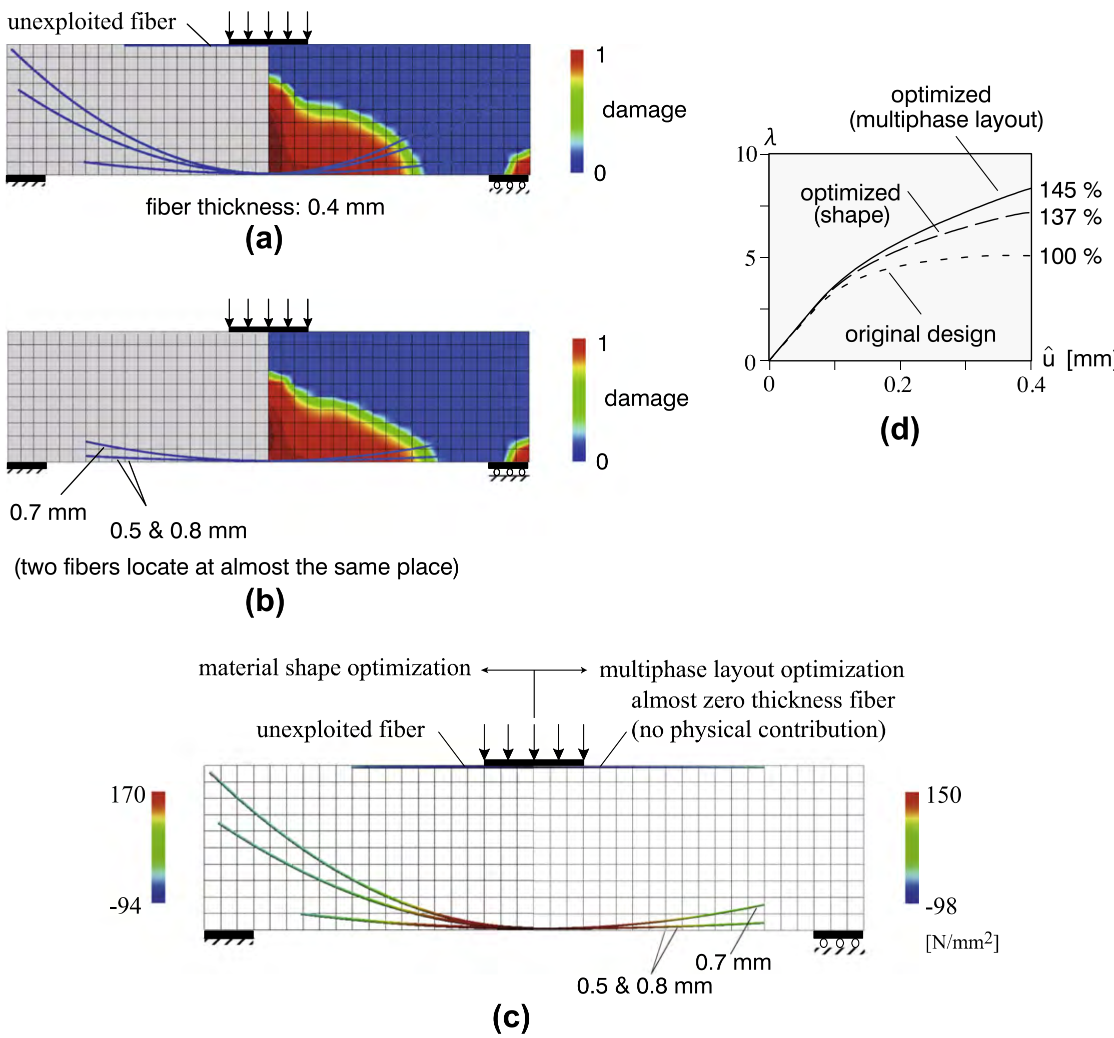


**Fig. 12.** Comparison of optimization results for deep beam, (a) optimized structure (material shape optimization), (b) optimized structure (2-phase layout optimization), (c) comparison of stress distribution of fiber, and (d) load-displacement curves.

optimization step number of 445 and 158, respectively. The right side of both Fig. 12a and b displays the damage distribution of concrete. In Fig. 12a the lower three fibers are shifted downward to prevent the concrete from a premature damage propagation after optimization. One upper fiber is also shifted upward to increase the bending stiffness of the beam although it is structurally not exploited [12]. The optimized fiber layout of Fig. 12a although being structurally feasible does not represent the global minimum, which is a consequence of the underlying non-convex optimization problem. In case of two-phase layout optimization the fiber material in the upper fiber moved to the lower fibers and the lower three fibers became thicker ($r_1 \approx 0.5$, 0.7, 0.8 mm) to resist the damage propagation, see Fig. 12b. Fig. 12c shows the comparison of stress distribution of the fibers after optimization between both kinds of optimization. Elastic limit tensile strength of fiber is 504 MPa (=Young's modulus $E$ (72.0 GPa) × $\kappa_0$ (0.007)), thus fibers are not yet damaged at this stage. The upper fiber shown in Fig. 12c (right) does not contribute to the mechanical response since the thickness is almost zero. As a result of the multiphase layout optimization, the structural ductility increases from 137% to 145%, see Fig. 12d.

*9.1.2. Splitting plate*

As the next comparison, the splitting plate with three AR-glass fibers is chosen as shown in Fig. 13a. Again the same material properties, loading condition, mesh and initial assumption of fiber geometry are used as in the previous example. 124 finite elements are used for concrete and 24 elements for the interface. For the present example the parametric element is restricted to the area below the cutout section, see Fig. 13a; this means that fibers cannot be located in the non-design space.

The initial set of the shape design variables is: (i) $s_{g1} = 0.025$ and (ii) $s_{g2}$ and $s_{g3}$ are 0.25, 0.50 or 0.75. The initial and the maximum fiber thicknesses are set to $r_1 = 0.5$ mm and $r_0 = 1.0$ mm, respectively, in multiphase layout optimization. Thus the initial set of the material design variables is $s_r = 0.5$ $(0 < s_r < 1)$ and the fiber thickness may vary within 0 mm < $r_1$ < 1.0 mm. The fiber volume is kept constant (0.74%) during the optimization. The prescribed displacement at control point $c$ is 0.2 mm.

Fig. 13b shows the result obtained by material shape optimization only whereas Fig. 13c is the result of two-phase layout optimization. Total optimization step numbers are 150 and 82, respectively. In Fig. 13b the middle fiber is also shifted to the upper part to resist the damage propagation of concrete together with the upper fiber. The location of the lower fiber stays in the lower part of the plate although one could expect that it also moves to the cutout area. Thus this fiber is mechanically unexploited. Anyhow an increase of 37% of structural ductility could be obtained by material shape optimization, see Fig. 13d. On the contrary, in Fig. 13c all fiber materials move to the upper edge. The lower fiber has almost zero thickness. Compared to the elastic tensile strength as introduced in the previous example, it is apparent that all fibers are not yet

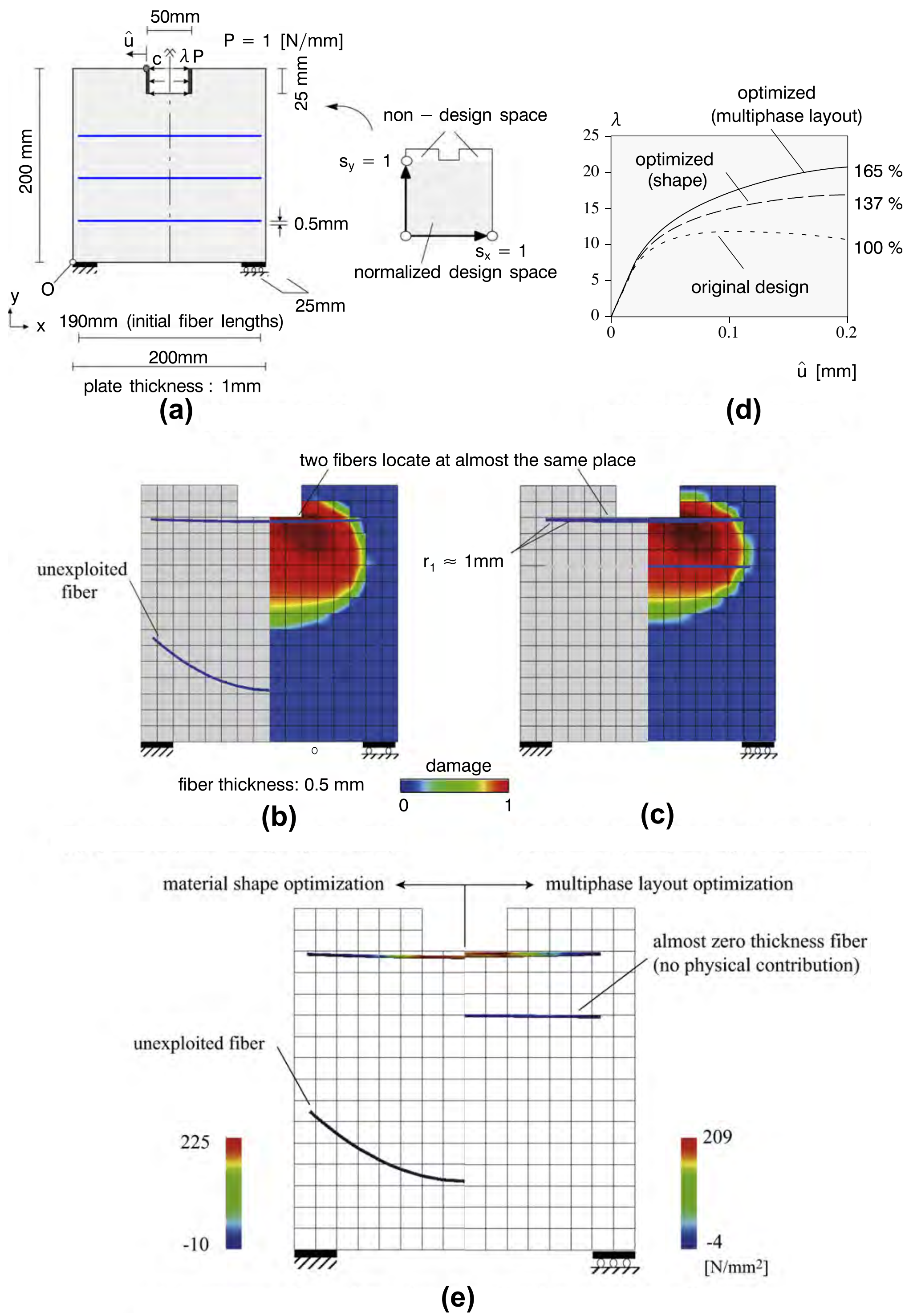


**Fig. 13.** Comparison of optimization results for splitting plate, (a) structural model, (b) optimized structure (material shape optimization), (c) optimized structure (2-phase layout optimization), (d) load-displacement curves, and (e) comparison of stress distribution of fiber.

damaged at this stage for both cases. For the multiphase layout optimization the structural ductility was further improved to 165%. It was verified by the above two comparisons that the proposed multiphase layout optimization can remedy the problem of 'unexploited' fibers; it avoids local the minima and provides further ductility than that of pure material shape optimization. In addition, it was shown from the two numerical examples that solution of multiphase layout optimization can be achieved with less total number of optimization steps than that of material shape optimization.

### 9.2. L-shape plate

As the final numerical example an L-shaped plate with two-phase fibers is chosen as displayed in Fig. 14b and the material properties are given in Fig. 14a. Plane stress conditions are assumed. 192 finite elements are used for concrete and 124 elements for the interface. In this example the geometry of the reinforcement is approximated by either horizontal or vertical straight fibers, see Fig. 14c. Each fiber has four design variables, i.e. three

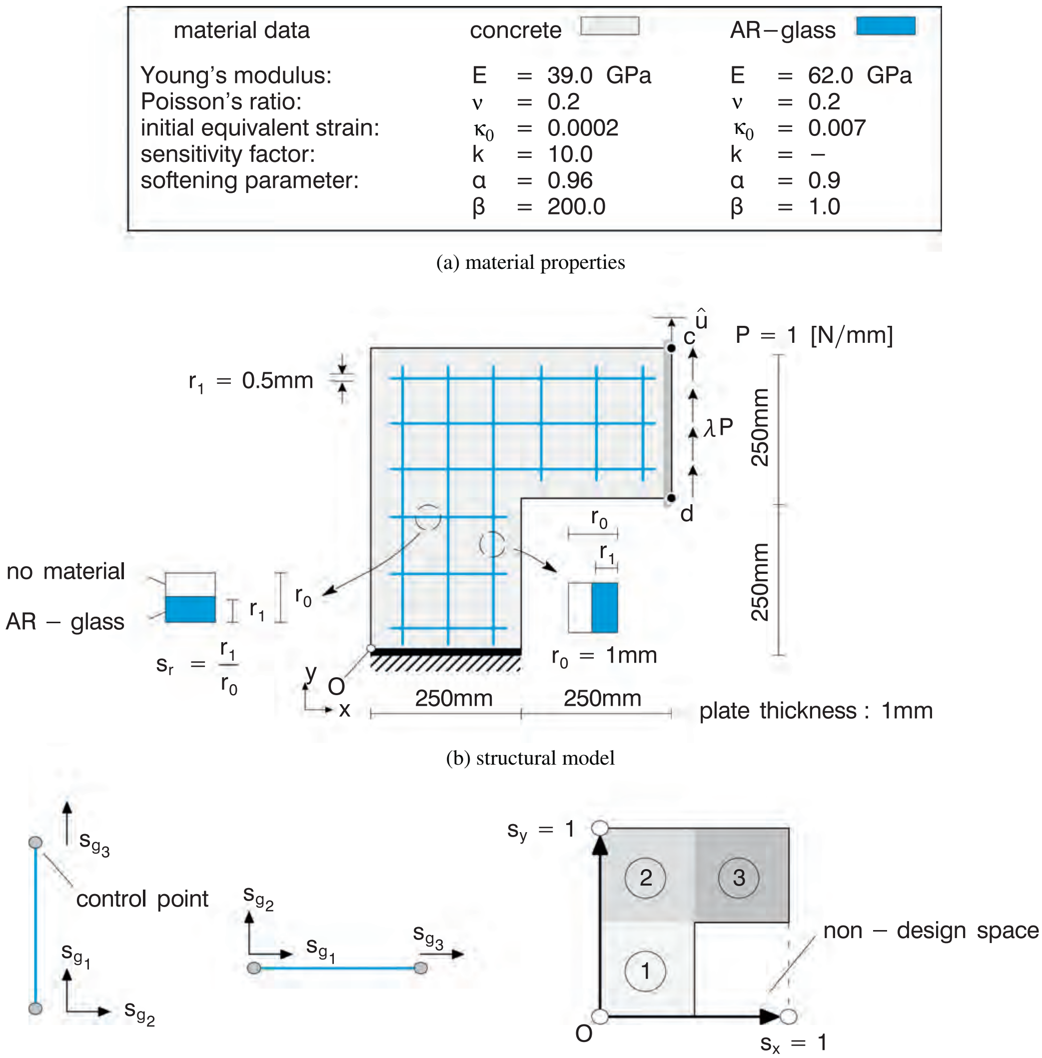


**Fig. 14.** Structural situation of L-shape plate.

shape design variables $s_g$ and one material design variable $s_r$. The total number of design variables is 48 (4 × 12 fibers).

The initial set of the shape design variables and their bounds are

(i) horizontal long fiber;
$s_{g_1} = 0.06,\ s_{g_3} = 0.94$ for all three fibers and $s_{g_2} = 0.6/0.75/0.9$,
$0.01 \leqslant s_{g_1} \leqslant 0.25, \quad 0.51/0.53/0.55 \leqslant s_{g_2} \leqslant 0.95/0.97/0.99,$
$0.75 \leqslant s_{g_3} \leqslant 0.99,$

(ii) horizontal short fiber;
$s_{g_1} = 0.06,\ s_{g_3} = 0.44$ for all three fibers and $s_{g_2} = 0.06/0.25/0.44$,
$0.01 \leqslant s_{g_1} \leqslant 0.1, \quad 0.01/0.03/0.05 \leqslant s_{g_2} \leqslant 0.95/0.97/0.99,$
$0.4 \leqslant s_{g_3} \leqslant 0.49,$

(iii) vertical long fiber;
$s_{g_1} = 0.001,\ s_{g_3} = 0.94$ for all three fibers and $s_{g_2} = 0.1/0.25/0.4$,
$0.001 \leqslant s_{g_1} \leqslant 0.0011,$
$0.01/0.03/0.05 \leqslant s_{g_2} \leqslant 0.45/0.47/0.49,\ 0.75 \leqslant s_{g_3} \leqslant 0.99,$

(iv) vertical short fiber;
$s_{g_1} = 0.56,\ s_{g_3} = 0.94$ for all three fibers and $s_{g_2} = 0.56/0.75/0.9$,
$0.51 \leqslant s_{g_1} \leqslant 0.6, \quad 0.01/0.03/0.05 \leqslant s_{g_2} \leqslant 0.95/0.97/0.99,$
$0.9 \leqslant s_{g_3} \leqslant 0.99.$

A thin concrete cover along to the structural boundary is allowed. Furthermore, slightly different lower and upper bounds are imposed to the three fibers in each group (i)–(iv) in order to avoid that some fibers concentrate at the same location in the vicinity of the structural boundary. Thus each $s_{g_2}$ has three kinds of bounds. Each fiber is continuously defined within two adjacent subspaces in the parametric element, see Fig. 14d, i.e. either '①–②' or '②–③', but not allowed to be in the remaining subspace ③ or ①, respectively. For example the lower horizontal short fiber, which is defined in the subspace ①, can move within the two subspaces '①–②' but cannot move into the subspace ③.

The initial fiber thickness is $r_1$ = 0.5 mm and the maximum thickness is prescribed by $r_0$ = 1.0 mm. Thus the initial set of the material design variables is $s_r$=0.5 for all fibers. The range of fiber thickness is 0 mm < $r_1$ < 1 mm. The lower and upper bounds for the material design variables $\mathbf{s}_r$ are defined as $s_L$ = 0.001 and $s_U$ = 0.99, respectively.

The analyses are carried out with a displacement controlled method; the control point $c$ is the upper right corner of the plate, see Fig. 14a. For comparison the structure is optimized based on either a linear elastic or a damage model. The prescribed nodal displacement $\hat{u}$ ($y$-direction) at the control point is 0.05 mm for the linear elastic case and either 1.5 mm or 3 mm for the damage case. The displacement is uniformly applied along the line between points *c* and *d*. The fiber volume is kept constant (1%) during the optimization.

Fig. 15a shows the optimized fiber layout and Fig. 15b is the stress distribution of one-dimensional fibers based on a linear elastic response. Since concrete gets easily damaged under small tension deformation, only small loading ($\hat{u} = 0.05$ mm) could be applied in order to ensure linear elastic response. Thus, the range of the axial stress of fiber is relatively small, see Fig. 15b. The elastic tensile strength of fiber is 434 MPa (=Young's modulus $E$ (62.0 GPa) $\times$ $\kappa_0$ (0.007)). Optimization was successful at the 394th step. After optimization, all long fibers are shifted to the structural boundary to increase the bending stiffness. Most of the fiber material in short fibers moved to the domain of the long fibers; thus the thickness $r_1$ of all long fibers reached the maximum size $r_0 = 1$ mm. This result is reasonable from structural point of view. As a result, 4% of ductility was increased.

Fig. 16 introduces the results of optimization based on a nonlinear structural response for the prescribed displacement $\hat{u} = 1.5$ mm. Fig. 16b is the damage distribution of the initial structure and Fig. 16c–e represents the optimized fiber layout, its damage distribution and stress distribution of fiber, respectively. In this case optimization was finished at the 136th step. In the initial

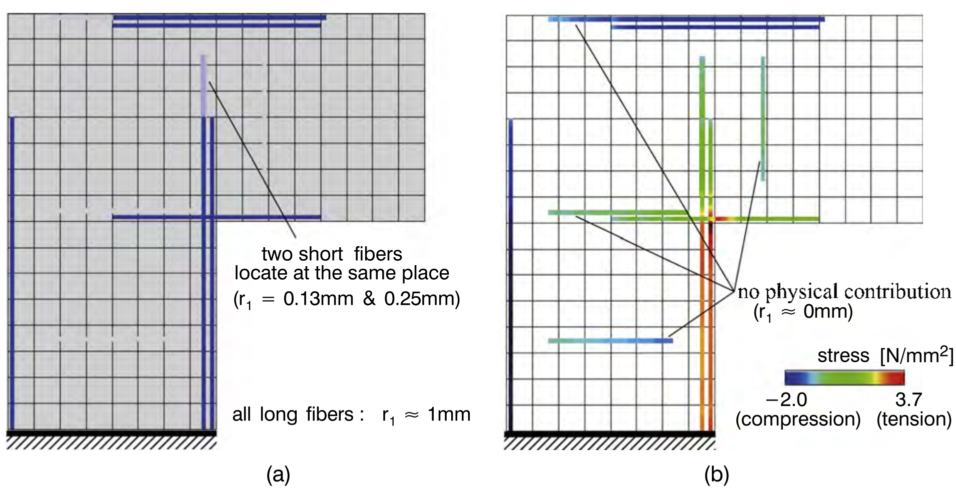


**Fig. 15.** Results of optimization for linear elastic response, (a) optimized fiber layout and (b) stress distribution of fibers.

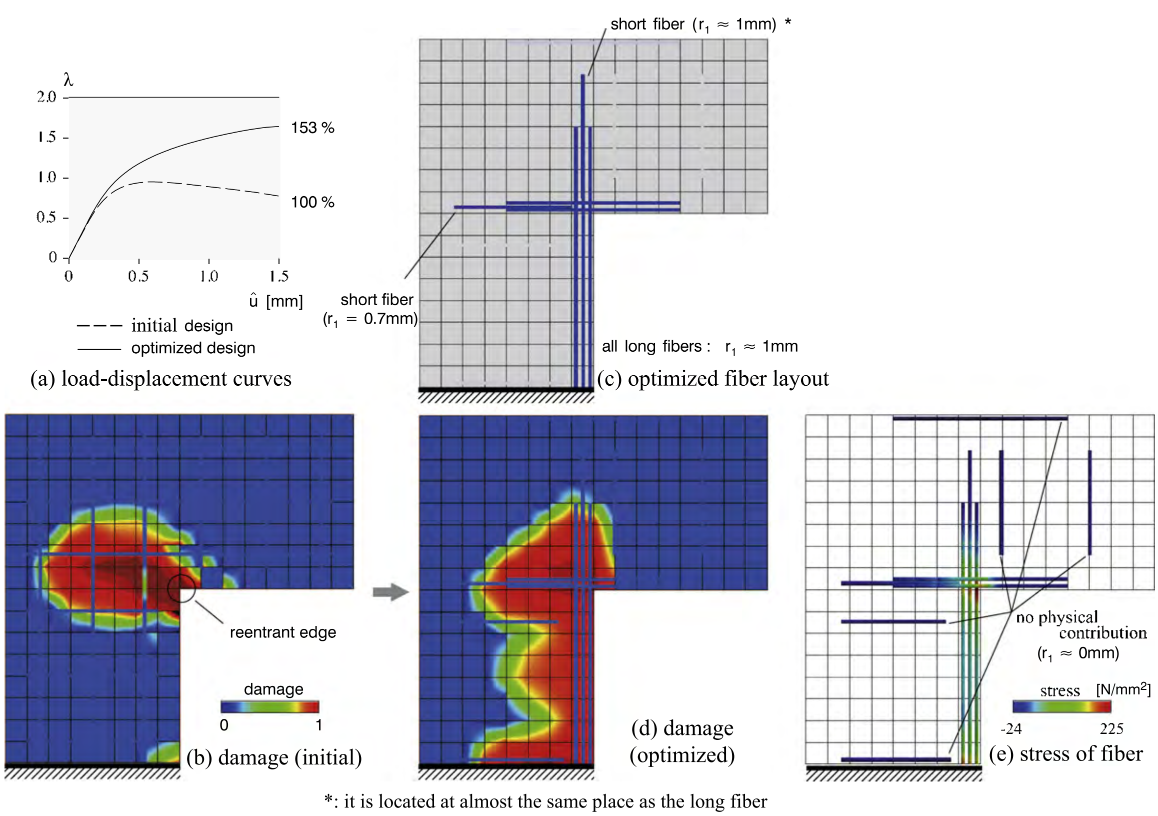


**Fig. 16.** Results of two-phase layout optimization for materially nonlinear response: (prescribed displacement $\hat{u} = 1.5$ mm), (a) load displacement curves, (b) damage distribution of initial structure, (c) fiber layout of optimized structure, (d) damage distribution of optimized structure, and (e) stress distribution of fiber.

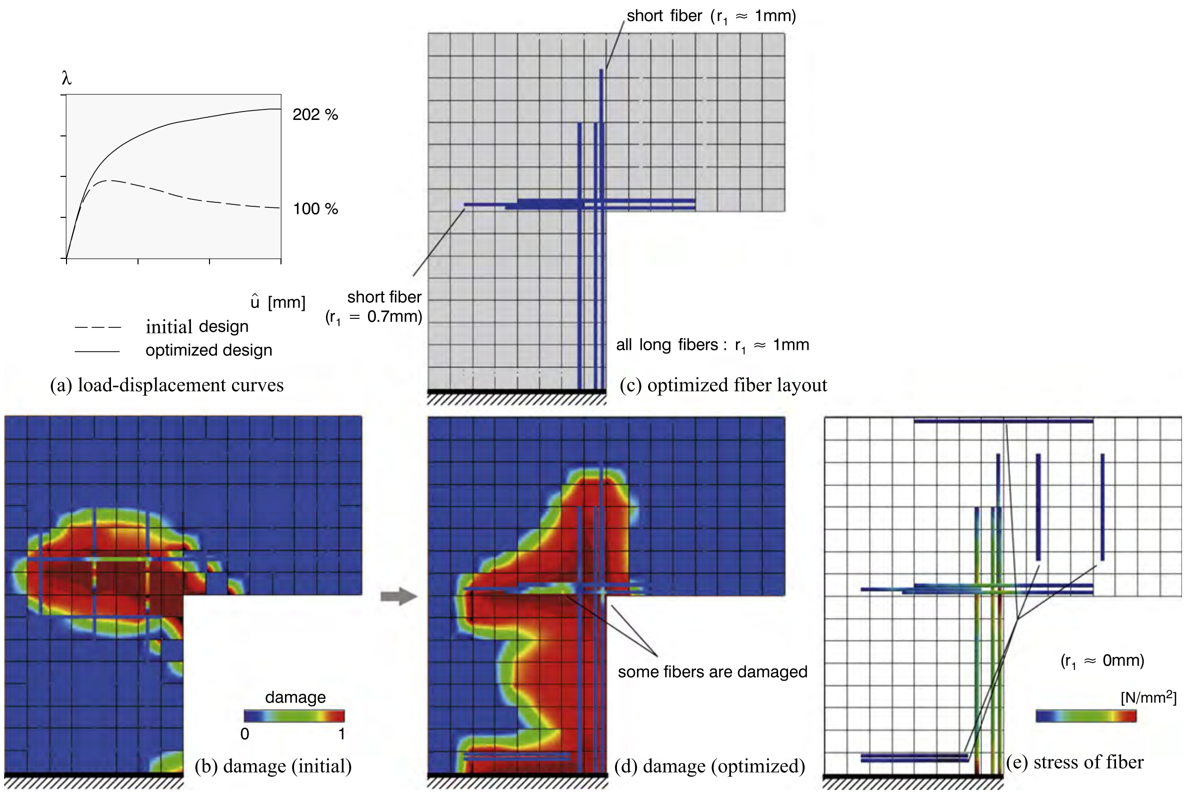


**Fig. 17.** Results of two-phase layout optimization for materially nonlinear response: (prescribed displacement $\hat{u} = 3$ mm), (a) load displacement curves, (b) damage distribution of initial structure, (c) fiber layout of optimized structure, (d) damage distribution of optimized structure, and (e) stress distribution of fiber.

structure the damage of concrete initiates at the reentrant corner and spreads mainly in the vicinity of the edge, see Fig. 16b. As can be seen in Fig. 16b, two horizontal long fibers moved to the lower part in order to reduce the damage in the vicinity of the reentrant corner; three vertical long fibers are shifted to the right side. Looking deeper at Fig. 16d, one can see that the damage of concrete in the optimized structure propagates entirely from the reentrant corner to the fixed boundary of the L-shape plate and the damage level is less than that of the initial structure. It can be recognized from Fig. 16d and e that although some fibers of the initial structure are damaged, all fibers of the optimized structure are still in the elastic range at this stage. As a result the structural ductility is increased by 53%, see Fig. 16a.

Analogously, Fig. 17 shows the results of optimization for the prescribed displacement $\hat{u} = 3$ mm. The total optimization step number was 209. Comparing Fig. 17b with Fig. 16b, one can observe that the initial structure fails with a distinct localization since the damage evolves only around the reentrant corner without distributing the stresses sufficiently to the other parts of the plate. The fiber layout of the optimized structure Fig. 17c shows a similar layout to that of Fig. 16c. However the response is different in that some fibers got damaged even in the final optimization stage; furthermore the left vertical long fiber is shifted to the inner part of the structure reducing the damage propagation of concrete. It can be recognized that some fibers are damaged for both the initial and the optimized structure at this stage, however level certainly decreases by obtaining the optimized fiber layout. The damage and stress distribution of fibers in Fig. 17d and e shows that severely damaged fiber material is in particular in the softening regime, and that its stress is below the elastic limit strength (434 MPa). This implies that the nonlinear structural response of FRC could be properly represented by the analyses. As a result the structural ductility could be increased by 102%, see Fig. 16a.

To summarize, it was verified that the proposed *multiphase layout optimization* has a great possibility to improve the ductility of FRC with a reasonable fiber layout.

## 10. Conclusions

A method for multiphase layout optimization was developed to maximize the structural ductility of Fiber Reinforced Composites such as FRC. For this objective it is of course mandatory to consider material nonlinearities. Therefore an isotropic gradient enhanced damage model is applied for both matrix (concrete) and fibers and a discrete bond model for the interface between matrix and fiber.

The proposed method combining multiphase material and material shape optimization previously separately applied allows for additional design freedom. The approach was able to remedy one of the problems of material shape optimization in which the effect of some fibers was not fully exploited. Thus this scheme can be denoted as a generalization of material optimization methods in that both 'material' and 'geometrical' design problems are solved simultaneously. Although the inclusion of different kinds of design variables often results in non-monotonic, sometimes highly nonlinear design functions with respect to the design variables, this problem could be solved by choosing a proper optimization method; in this study the MMA provided reliable optimization solutions.

The performance of the proposed method was demonstrated by numerical examples; it was shown that the 'unexploited fibers' recognized in material shape optimization vanished successfully so that the ductility could be further increased. The increase of ductility is in particular important for situations where sufficient energy absorption plays a substantial role, as for example under earthquake excitation.

## Acknowledgement

The present study is supported by Grants of the "Deutsche Forschungsgemeinschaft" DFG (German Research Foundation) within the research Projects Ra 218/19 and Ra 218/21. This support is gratefully acknowledged.

## Appendix A. List of symbols

The following list of symbols is added for a better understanding of the notation used in the text.

| | |
|---|---|
| $(\bullet)^{(n)}$ | iteration index in path-dependent algorithms |
| $(\bullet)_t$, $(\bullet)_{t+1}$ | values at reference and actual time step, respectively |
| $(\bullet)_e$ | values on element level |
| $(\bullet)^x$, $(\bullet)^y$ | vector component of $x$- and $y$-direction, respectively |
| $(\bullet)^c$, $(\bullet)^f$, $(\bullet)^i$ | term related to concrete matrix, fiber and interface between matrix and fiber, respectively |
| $(\bullet)^{c+f}$ | term relevant to concrete matrix and fiber |
| $\delta(\bullet)$, $d(\bullet)$, $\Delta(\bullet)$ | variation, infinitesimal increment, increment value, respectively |

*Gradient operators, mathematical function*

| | |
|---|---|
| $\nabla_s(\bullet)$ | partial derivatives with respect to an optimization variable $\hat{s}_i$, regarding other variables $\hat{s}_j$ for $j \neq i$ as constant |
| $\nabla_s^{\mathrm{ex}}(\bullet)$ | explicit part of partial derivatives $\nabla_s(\bullet)$ |
| $\nabla^2$ | Laplacean operator |
| $\langle\bullet\rangle$ | macauley bracket: $\langle x \rangle = (x + \vert x \vert)/2$ |

*Optimization values, functions*

| | |
|---|---|
| $s$, $\hat{\mathbf{s}}$ | design function (design variable) and vector of optimization variables, respectively |
| $s_r$, $\hat{\mathbf{s}}_r$ | design function for material design and vector of material design variables, respectively |
| $s_g$, $\hat{\mathbf{s}}_g$ | design function for shape design and vector of shape design variables, respectively |

*Geometry*

| | |
|---|---|
| $\mathbf{N}$, $\widetilde{\mathbf{N}}$, $\overline{\mathbf{N}}$ | shape function for displacement, non-local equivalent strain, interfacial slip field, respectively |

*Kinematic measures*

| | |
|---|---|
| $u_L$ | local displacement field along axis of one-dimensional fiber |
| $\boldsymbol{\varepsilon}_L$, $\varepsilon_L$ | strain tensor in local coordinate system and local strain field along axis of fiber, respectively |
| $\boldsymbol{\varepsilon}_{\mathrm{pre}}$ | prescribed strain |
| $\mathbf{e}$ | nodal non-local strain vector |
| $\bar{\mathbf{d}}$ | nodal slip vector (nodal relative displacement vector) |
| $\mathbf{B}$, $\widetilde{\mathbf{B}}$, $\overline{\mathbf{B}}$ | discretized constant differential operator for displacement, non-local equivalent strain interfacial slip field, respectively |

*Forces, loads, stresses*

| | |
|---|---|
| $\boldsymbol{\sigma}_L$, $\sigma_L$ | Cauchy stress tensor in local coordinate system and local stress along axis of fiber, respectively |
| $\hat{\mathbf{t}}$, $\mathbf{t}_0$ | prescribed surface traction vector and reference surface traction vector, respectively |
| $\mathbf{f}_{\mathrm{int}}$, $\mathbf{f}_{\mathrm{ext}}$ | internal vector and external force vector, respectively |

*Materials*

| | |
|---|---|
| $\mathbb{C}_{\mathrm{eff}}, \mathbb{C}_{\mathrm{ed}}, \mathbb{C}_T$ | effective material stiffness tensor or matrix, elasto-damage secant material stiffness tensor or matrix, tangential material stiffness tensor or matrix, respectively |
| $\mathbf{T}^d$, $\mathbf{T}^\varepsilon$, $\mathbf{T}^\sigma$ | rotation matrix, strain transformation matrix, stress transformation matrix, respectively |
| $\eta, \hat{\eta}$ | penalization factor and fitting parameter, respectively |
| $u_1^i, u_2^i, u_3^i$ | slip length defining change of interfacial behavior |
| $k_L$ | tangential stiffness of interface |
| $\sigma_{m,0}$, $\sigma_m$ | initial and current adhesion strength |
| $\sigma_{f,0}$, $\sigma_f$ | initial and current sliding friction strength |
| $r_s$, $h_s$ | radius and surface roughness of a fiber, respectively |
| $\alpha_r$, $\alpha_f$ | constants assuming lateral deformation of fiber |
| $f_c$ | uniaxial compressive strength of concrete |
| $\varepsilon_s$ | uniaxial strain of fiber |
| $R_s$ | radius of curvature at slip $u_1^i$ |
| $\sigma_R$ | stress perpendicular to fiber |

## References

[1] Balakrishnan S, Murray DW. Finite element prediction of reinforced concrete behavior. Structural engineering report no. 138, University of Alberta, Edmonton, Alberta, Canada; 1986.
[2] Bendsøe MP, Neves MM, Sigmund O. Some recent results on topology optimization of periodic composites. In: Proceedings of the NATO advanced research workshop on topology optimization of structures and composite continua, Budapest, Hungary; 2000. p. 3–17.
[3] Bendsøe MP, Sigmund O. Topology optimization theory method and applications. Berlin/Heidelberg/New York: Springer-Verlag; 2003.
[4] Brameshuber W, Brockmann T, Hegger J, Molter M. Untersuchungen zum textilbewehrten Beton. Beton 2002;52:424–9.
[5] Curbach M, Jesse F. Eigenschaften und anwendung von textilbeton. Beton Stahlbet 2009;104 Heft 1:16–9.
[6] Gibson LJ, Ashby MF. Cellular solids: structure and properties. Cambridge (UK): Cambridge University Press; 1999.
[7] Hegger J, Voss S. Investigations on the bearing behaviour and application potential of textile reinforced concrete. Eng Struct 2008;30:2050–6.
[8] Hund A. Mehrskalenmodellierung des versagens von werkstoffen mit mikrostruktur. PhD thesis, Institut für Baustatik, Universität Stuttgart, Germany; 2007. <http://www.ibb.uni-stuttgart.de/publikationen/index.en.html>.
[9] Kato J, Lipka A, Ramm E. Preliminary investigation for optimization of fiber reinforced cementitious composite structures. In: Mota Soares CA et al., editors. Proceedings of 3rd European conference on computational mechanics, solids, structures and coupled problems in engineering, ECCM, Lisbon, Portugal; 2006.
[10] Kato J. Material Optimization for fiber reinforced composites applying a damage formulation. PhD thesis, Institut für Baustatik und Baudynamik, Universität Stuttgart, Germany; 2010. <http://www.ibb.uni-stuttgart.de/publikationen/index.en.html>.
[11] Kato J, Lipka A, Ramm E. Multiphase material optimization for fiber reinforced composites with strain softening. Struct Multidisc Optim 2009;39:63–81.
[12] Kato J, Ramm E. Optimization of fiber geometry for fiber reinforced composites considering damage. Finite Elem Anal Des 2010;46:401–15.
[13] Krüger M, Ozbolt J, Reinhardt HW. A discrete bond model for 3D analysis of textile reinforced and prestressed concrete elements. Otto-Graf-J 2002;13:111–28.

[14] Krüger M, Ozbolt J, Reinhardt HW. A new 3D discrete bond model to study the influence of bond on the structural performance of thin reinforced and prestressed concrete plates. In: Reinhardt HW et al., editors. Proceedings of high performance fiber reinforced cement composites (HPFRCC4). Ann Arbor (USA): RILEM; 2003. p. 49–63.

[15] Krüger M, Xu S, Reinhardt HW, Ozbolt J. Experimental and numerical studies on bond properties between high performance fine grain concrete and carbon textile using pull out tests, In: Beiträge aus der Befestigungstechnik und dem Stahlbetonbau, Festschrift Professor R. Eligehausen Universität Stuttgart, Germany; 2002. p. 151–64.

[16] Lipka A. Verbesserter materialeinsatz innovativer werkstoffe durch die topologieoptimierung. PhD thesis, Institut für Baustatik und Baudynamik, Universität Stuttgart, Germany; 2007. <http://www.ibb.uni-stuttgart.de/publikationen/index.en.html>.

[17] Lipka A, Ramm E. Optimization of foam filled structures using gradient algorithms. In: Bendsøe MP et al., editors. Proceedings of the IUTAM SYMPOSIUM: topoptSymp2005. Topological design optimization of structures, machines and materials status and perspectives, Copenhagen, Denmark; 2005. p. 319–29.

[18] Lipka A, Ramm E. A concept for the optimization of structures with foam cores. In: Herskovits J et al., editors. Proceedings of the 6th world congress on structural and multidisciplinary optimization, WCSMO-6, Rio de Janeiro, Brazil; 2005.

[19] Maute K. Topologie- und formoptimierung von dünnwandigen tragwerken. PhD thesis, Institut für Baustatik, Universität Stuttgart, Germany; 1998. <http://www.ibb.uni-stuttgart.de/publikationen/index.en.html>.

[20] Maute K, Schwarz S, Ramm E. Adaptive topology optimization of elastoplastic structures. Struct Optim 1998;15:81–91.

[21] Mazars J, Pijaudier-Cabot G. Continuum damage theory – application to concrete. J Eng Mech 1989;115:345–65.

[22] Olhoff N, Rasmussen J. Study of inaccuracy in semi-analytical sensitivity analysis – a model problem. Struct Optim 1991;3:203–13.

[23] Olhoff N, Rasmussen J, Lund E. A method of exact numerical differentiation for error elimination in finite-element-based semi-analytical shape sensitivity analysis. Mech Struct Mach 1993;21(1):1–66.

[24] Peerlings RHJ, de Borst R, Brekelmans WAM, de Vree JHP. Gradient enhanced damage for quasi-brittle materials. Int J Numer Methods Eng 1996;39:3391–403.

[25] Peerlings RHJ, de Borst R, Brekelmans WAM, Geers MGD. Gradient-enhanced damage modelling of concrete fracture. Mech Cohes Frict Mater 1998;3:323–42.

[26] Peerlings RHJ. Enhanced damage modelling for fracture and fatigue. PhD thesis, Technische Universiteit Eindhoven, The Netherlands; 1999.

[27] Schladitz F, Frenzel M, Ehlig D, Curbach M. Bending load capacity of reinforced concrete slabs strengthened with textile reinforced concrete. Eng Struct 2008;40:317–26.

[28] Sigmund O, Torquato S. Design of materials with extreme thermal expansion using a three-phase topology optimization method. J Mech Phys Solids 1997;45(6):1037–67.

[29] Stegmann J, Lund E. Discrete material optimization of general composite shell structures. Int J Numer Methods Eng 2005;62:2009–27.

[30] Stolpe M, Stegmann J. A Newton method for solving continuous multiple material minimum compliance problems. Struct Multidisc Optim 2008;35:93–106.

[31] Svanberg K. A class of globally convergent optimization methods based on conservative convex separable approximations. SIAM J Optim 2002;12(2):555–73.

[32] de Vree JHP, Brekelmans WAM, Gils MAJ. Comparison of nonlocal approaches in continuum damage mechanics. Comput Struct 1995;55:581–8.

[33] Xu S, Krüger M, Reinhardt HW, Ozbolt J. Bond characteristics of carbon, alkali resistance glass, and aramid textiles in mortar. J Mater Civil Eng ASCE 2004;16(4):356–64.

[34] Zhou M, Rozvany GIN. The COC algorithm, part II: topological, geometrical and generalized shape optimization. Comput Methods Appl Mech Eng 1991;89:309–36.